



A finite element model for shape memory alloys considering thermomechanical couplings at large strains

Daniel Christ*, Stefanie Reese

Institute of Solid Mechanics, TU Braunschweig, Schleinitzstr. 20, D-38106 Braunschweig, Germany

ARTICLE INFO

Article history:

Received 26 February 2009

Received in revised form 15 April 2009

Available online 27 June 2009

Keywords:

Phase transformation

Thermomechanical processes

Constitutive behaviour

Finite strain

Finite elements

ABSTRACT

In the present work we propose a new thermomechanically coupled material model for shape memory alloys (SMA) which describes two important phenomena typical for the material behaviour of shape memory alloys: pseudoelasticity as well as the shape memory effect. The constitutive equations are derived in the framework of large strains since the martensitic phase transformation involves inelastic deformations up to 8%, or even up to 20% if the plastic deformation after the phase transformation is taken into account. Therefore, we apply a multiplicative split of the deformation gradient into elastic and inelastic parts, the latter concerning the martensitic phase transformation. An extended phase transformation function has been considered to include the tension–compression asymmetry particularly typical for textured SMA samples. In order to apply the concept in the simulation of complex structures, it is implemented into a finite element code. This implementation is based on an innovative integration scheme for the existing evolution equations and a monolithic solution algorithm for the coupled mechanical and thermal fields. The coupling effect is accurately investigated in several numerical examples including pseudoelasticity as well as the free and the suppressed shape memory effect. Finally, the model is used to simulate the shape memory effect in a medical foot staple which interacts with a bone segment.

© 2009 Elsevier Ltd. All rights reserved.

1. Introduction

In the last years smart materials have attracted much attention, especially because of their versatile application in smart structures, medical devices and actuator systems (e.g. Van Humbeeck, 2001; Fu et al., 2004; Morgan, 2004). Among these materials, shape memory alloys, particularly Nickel–Titanium (NiTi) belong to the most established. In comparison to other metallic materials they exhibit large inelastic recoverable strains (of the order of 8%) resulting from the transformation between austenitic and martensitic phases (see Otsuka and Wayman, 1999). This transformation may be induced by a change either in the applied stress, the temperature, or in a combination of both.

From the macroscopic point of view, the behaviour of shape memory alloys exhibits two major phenomena. The first one is known as pseudoelasticity which is characterised by nonlinearly elastic behaviour. Here, very large strains upon loading occur but full recovery is achieved in a hysteresis loop upon unloading. The shape memory effect, on the other hand, is accompanied by large residual strains after loading and subsequent unloading. These strains are due to the orientation of martensite twins (pseudoplasticity). They may be fully recovered simply by raising the temper-

ature of the body. Additionally, these materials exhibit full thermomechanical coupling. Thus, the temperature of the alloy changes upon applied force, and the mechanical response changes upon temperature deviation.

During the last decade the area of constitutive modelling of shape memory alloys (SMA) has been the topic of many research publications. The majority of the published material models can be classified into three different groups: micromechanically based approaches, concepts based on statistical thermodynamics and phenomenological models. Since we already reviewed the three groups in detail (Reese and Christ, 2008), we now concentrate on a literature overview of phenomenological models for shape memory alloys. We subdivide them into models for the different phenomena pseudoelasticity and the shape memory effect as well as finally the tension–compression asymmetry. We also present existing models which are derived in the framework of large strains. After all, the implementation of the material models into a finite element code is surveyed. If the reader is interested in further research on this topic we recommend Roubicek (2005) and Patoor et al. (2006) who give a detailed overview of micromechanical modelling of shape memory alloys. Lagoudas et al. (2006) provide a survey of constitutive formulations for polycrystalline shape memory alloys where a distinction between the micromechanical and the phenomenological approach is made.

* Corresponding author.

E-mail address: d.christ@tu-bs.de (D. Christ).

The most common material laws for shape memory alloys are able to describe the effect of pseudoelasticity. In the 1980s (e.g. Tanaka, 1986) and in the 1990s (e.g. Raniecki et al., 1992; Brinson, 1993) one-dimensional constitutive models were already proposed to describe the hysteretical behaviour of shape memory alloys during the phase transformation from austenite to martensite. From the late 1990s three-dimensional concepts were developed. Most of these approaches are structured similarly. They are based on a macroscopic free energy function (either Gibbs free energy or Helmholtz free energy) which includes internal variables to describe the phase transformation. In general, one scalar variable, the martensitic volume fraction, defines the progress of the phase transformation and determines its end. Raniecki et al. (1992) among others derived a relation between the martensitic volume fraction and the inelastic strain occurring during the phase transformation. By defining the martensitic volume fraction via a norm of the transformation strain tensor, the three-dimensional character of the phase transformation is considered (e.g. Raniecki and Lexcellent, 1994; Boyd and Lagoudas, 1996).

Patoor et al. (1987) and Achenbach (1989) were the first to suggest an additive decomposition of the martensitic volume fraction into different variants. Brinson (1993) has introduced this concept into the phenomenological material modelling. The motivation for this idea was to introduce the so-called temperature induced martensite (also known as self-accommodated martensite) which serves to include the shape memory effect into the material model. The idea of the additive split of the martensitic volume fraction was further developed by, for example, Leclercq and Lexcellent (1996), Lexcellent et al. (2002), Souza et al. (1998), Helm and Haupt (2003), Christ et al. (2004), Auricchio and Petrini (2004a), Paiva et al. (2005) and Popov and Lagoudas (2007).

Since the shape memory effect originates from stress orientation of the martensite twins and subsequent heating, the temperature plays an important role. The simplest way to include the temperature in the modelling is to hold it fixed at each point of the structure and to assume a homogeneous temperature field. This would result in a one-sided thermomechanical coupling where only the influence of the temperature on the deformation is taken into account. But important physical effects as heat conduction and heat generation due to energy dissipation during the phase transformation, can only be considered if full thermomechanical coupling (including the solution of the first law of thermodynamics) is incorporated. The finite element implementation of thermomechanically coupled models were accomplished by Lim and McDowell (2002), Auricchio and Petrini (2004b), Migliavacca et al. (2004), Iadicola and Shaw (2004), Popov and Lagoudas (2007) and Helm (2007b). However, all publications mentioned are limited to small strains.

Phenomenological large strain concepts were proposed by Levitas (1998), Auricchio and Taylor (1997), Masud et al. (1997), Idesman et al. (1999), Auricchio (2001), Anand and Gurtin (2003), Müller and Bruhns (2006), Vieille et al. (2007), Ziolkowski (2007), Helm (2007a) and Reese and Christ (2008). Thermomechanical coupling is additionally included in the models of Müller and Bruhns (2006) and Ziolkowski (2007). Particularly the concepts of Auricchio and Taylor (1997), Auricchio (2001), Vieille et al. (2007) and Reese and Christ (2008) focus on the finite element implementation of the constitutive model. The above mentioned articles do not focus on the shape memory effect. Hence, it seems that none of the presented models is fully capable of combining all important features as pseudoelasticity, the shape memory effect, thermomechanical coupling and finite deformations in only one model and additionally offers an efficient and robust finite element implementation.

In the present work we seek to make another step forward on this way. For this purpose, we enhance the model proposed in

Reese and Christ (2008) by an additive split of the martensitic volume fraction z into an oriented martensite fraction z_o and an unoriented martensite z_u , also known as self-accommodated martensite. The split allows us to describe the martensite orientation below the martensite finish temperature as well as the thermally driven phase transformation from oriented martensite to austenite by heating above the austenite start temperature A_s . Additionally, we extend the approach to thermomechanical coupling by applying the balance of internal energy. Hence, an interaction between the mechanical and the thermal quantities is enabled. The model is derived in the framework of large strains based on the multiplicative decomposition of the deformation gradient into an elastic part and a transformation part where the latter stands for the inelastic deformation produced during the phase transformation or the orientation of martensite twins, respectively. The numerical implementation of this model is carried out by means of an integration algorithm based on the exponential map which preserves the volume during the phase transformation.

2. Kinematic framework

2.1. Deformation gradients

The proposed material model is derived in the framework of finite deformations. This implies the use of the deformation gradient $\mathbf{F} = \partial \mathbf{x} / \partial \mathbf{X}$, where the vector $\mathbf{x} = \mathbf{x}(\mathbf{X}, t)$ (t : time) denotes the position of a point in the current configuration and \mathbf{X} the position of the same point in the reference configuration. The determinant of the deformation gradient $J = \det \mathbf{F}$ describes the volume change of the material during the deformation. As in classical plasticity, we assume an intermediate state which is stress free and decouples the elastic deformation from the deformation during the martensitic phase transformation $\mathbf{F}_t = \mathbf{F}_e^{-1} \mathbf{F}$. The subscript e stands for the elastic deformation and t for the transformation part. As shown in earlier investigations (e.g. Fu et al., 1992) the phase transformation in polycrystalline shape memory alloys does not emerge spontaneously. During the forward transformation the stress is slightly increasing whereas during the backward transformation the stress is decreasing. This characteristic can be described phenomenologically by introducing an additional deformation gradient $\mathbf{F}_{td} = \mathbf{F}_{te}^{-1} \mathbf{F}_t$ which is multiplicatively coupled to the deformation during the phase transformation. Since the phase transformation in NiTi approximately proceeds without a volume change (see Bhattacharya, 1992), the determinant of the transformation deformation gradient $J_t = \det \mathbf{F}_t$ has to remain unchanged so that $J_t \equiv 1$ holds.

It should be emphasised that the triple multiplicative split $\mathbf{F} = \mathbf{F}_e \mathbf{F}_{te} \mathbf{F}_{td}$ has been used already several times, for the first time probably in the work of Lion (2000) to model kinematic hardening, see also Dettmer and Reese (2004), Vladimirov et al. (2008). According to Lion (2000) the elastic part of the inelastic deformation (in the present contribution denoted by \mathbf{F}_{te}) results from dislocation-induced lattice rotations and stretches on the microscale, whereas the inelastic part (here defined by \mathbf{F}_{td}) relates to local plastic deformations coming from inelastic slip on crystallographic slip systems. Helm (2007a) suggests to transfer the idea of the triple multiplicative split on phase transformations. The same approach is taken by Reese and Christ (2008).

2.2. Strain tensors and its time derivatives

Since the deformation gradient \mathbf{F} is not a suitable strain measure we use the Green–Lagrange strain tensor $\mathbf{E} = (\mathbf{C} - \mathbf{1})/2$, where $\mathbf{C} = \mathbf{F}^T \mathbf{F}$ denotes the right Cauchy–Green tensor. In the same manner we introduce the transformation strain tensor

$\mathbf{E}_t = (\mathbf{C}_t - \mathbf{1})/2 = (\mathbf{F}_t^T \mathbf{F}_t - \mathbf{1})/2$. In addition to \mathbf{E}_t , we use the elastic right Cauchy–Green tensor $\mathbf{C}_e = \mathbf{F}_e^T \mathbf{F}_e = \mathbf{F}_t^T \mathbf{C} \mathbf{F}_t^{-1}$ and its transformation counterpart $\mathbf{C}_{te} = \mathbf{F}_{te}^T \mathbf{F}_{te} = \mathbf{F}_{td}^T \mathbf{C}_t \mathbf{F}_{td}^{-1}$. For further use we define the time derivatives of the right Cauchy–Green tensors

$$\dot{\mathbf{C}}_e = -\mathbf{L}_t^T \mathbf{C}_e + \mathbf{F}_t^{-T} \dot{\mathbf{C}} \mathbf{F}_t^{-1} - \mathbf{C}_e \mathbf{L}_t, \quad (1)$$

$$\dot{\mathbf{C}}_{te} = -\mathbf{L}_{td}^T \mathbf{C}_{te} + \mathbf{F}_{td}^{-T} \dot{\mathbf{C}}_t \mathbf{F}_{td}^{-1} - \mathbf{C}_{te} \mathbf{L}_{td} \quad (2)$$

with $\mathbf{L}_t := \dot{\mathbf{F}}_t \mathbf{F}_t^{-1}$ and $\mathbf{L}_{td} := \dot{\mathbf{F}}_{td} \mathbf{F}_{td}^{-1}$. Their symmetric parts are given by $\mathbf{d}_t = (\mathbf{F}_t^{-T} \dot{\mathbf{C}}_t \mathbf{F}_t^{-1})/2$ and $\mathbf{d}_{td} = (\mathbf{F}_{td}^{-T} \dot{\mathbf{C}}_{td} \mathbf{F}_{td}^{-1})/2$, respectively.

3. Continuum mechanical model

3.1. Free energy function

Choosing the correct form of the free energy is a fundamental problem of the thermodynamics of phase transformations. The function must cover the main properties of shape memory alloys. The material consists of at least two different phases, martensite (M) and austenite (A). During the phase transformation strong thermomechanical coupling occurs. Thus, in addition to the deformation, the temperature plays a very important role. As a first step, we propose the total Helmholtz free energy Ψ per reference volume as a combination of an elastic part Ψ_e and a transformation part Ψ_t as suggested by Helm and Haupt (2003). We assume that the elastic part depends on the elastic right Cauchy–Green tensor \mathbf{C}_e , the martensitic volume fraction z and the temperature $\theta = \theta(\mathbf{X}, t)$. The transformation part only depends on \mathbf{C}_{te} since we assume that the internal dislocations and inclusions in the crystal lattice are neither affected by the phase transformation nor by a temperature influence. We finally obtain

$$\Psi = \Psi_e(\mathbf{C}_e, z, \theta) + \Psi_t(\mathbf{C}_{te}). \quad (3)$$

The elastic part of the free energy Ψ_e includes the elastic energy of the austenitic and martensitic phase coupled to the martensitic volume fraction z . The mixture is defined by

$$\Psi_e(\mathbf{C}_e, \theta, z) = (1 - z) \Psi_e^A(\mathbf{C}_e, \theta) + z \Psi_e^M(\mathbf{C}_e, \theta). \quad (4)$$

The martensitic volume fraction varies between 0 and 1. In case of $z = 0$, the material is purely austenitic and in case of $z = 1$ purely martensitic. The different phase energies Ψ_e^A and Ψ_e^M are chosen as isotropic functions of the right Cauchy–Green tensor \mathbf{C}_e and θ :

$$\begin{aligned} \Psi_e^{A/M} = & \frac{\mu^{A/M}}{2} (I_{C_e} - 3 - 2 \ln J_e) + \frac{\lambda^{A/M}}{4} (J_e^2 - 1 - 2 \ln J_e) \\ & - 3 \alpha_T^{A/M} (\theta - \theta_0) \left(\lambda^{A/M} + \frac{2}{3} \mu^{A/M} \right) \frac{\ln J_e}{J_e} \\ & + c_d^{A/M} \left(\theta \left(1 - \ln \frac{\theta}{\theta_0} \right) - \theta_0 \right) + e_0^{A/M} - \theta \eta_0^{A/M}. \end{aligned} \quad (5)$$

The superscript A/M stands for the separate phases (A: austenite, M: martensite). The function consists of three parts. The first line in (5) represents the part depending only on the strain measure \mathbf{C}_e (I_{C_e} is the first invariant of \mathbf{C}_e and the determinant $J_e = \det \mathbf{F}_e$ can be rewritten as $J_e = \sqrt{\text{III}_{C_e}}$, i.e. is a function of the third invariant of \mathbf{C}_e). It is chosen as the hyperelastic potential for Neo-Hookean elasticity including the Lamé constants μ and λ for each phase, respectively. The term in the second line stands for the so-called thermoelastic effect which describes the correlation between the temperature and a volume change in the material. Thus, the chosen function depends on θ and J_e . The parameter θ_0 refers to the initial temperature and the material parameter α_T is the thermal expansion coefficient. The terms in the third line only depend on the temperature θ and some additional material parameters, the heat capacity c_d , the internal energy $e(\theta_0) = e_0$ and the entropy $\eta(\theta_0) = \eta_0$ of the respective phases A and M. Already at this state

of the derivation we like to emphasise that the terms $e_0^{A/M}$ and $\eta_0^{A/M}$ do not enter the final modelling equations separately. Only the differences $\Delta e_0 := e_0^M - e_0^A$ and $\Delta \eta_0 := \eta_0^M - \eta_0^A$ need to be defined for the simulation. Both expressions, Δe_0 and $\Delta \eta_0$, are in general functions of \mathbf{C}_e . We follow the common strategy (refer, for example, to Huo and Müller (1993)) and treat them as material parameters (see also Section 3.3 and Table 1). Note that the values of the material parameters Δe_0 and $\Delta \eta_0$ already imply the density of NiTi (with $\rho_0 = 6400 \text{ kg/m}^3$) and have therefore the dimension [MPa] and [MPa/K], respectively.

It can be easily shown that for the assumption of small strains the free energy function (5) and its derivatives coincide with the classical functions depending on the linearised strain $\mathbf{e}_e = \mathbf{e} - \mathbf{e}_t$ and the temperature.

The second part of the total free energy Ψ_t describes one part of the energy storage during the phase transformation. This part depends on the strain measure \mathbf{C}_{te} . The function is chosen as

$$\Psi_t = \frac{\mu_t}{2} (I_{C_{te}} - 3) \quad (6)$$

where μ_t is another material parameter and $I_{C_{te}}$ is the first invariant of \mathbf{C}_{te} .

Note that Ψ_t has mainly phenomenological character. It merely serves to model the hysteresis in the stress–strain response more accurately and should not be confused with the so-called coherency energy introduced by Müller and Xu (1991). Since we work with a purely continuum mechanical model we do not incorporate the crystal structure and the different geometrical shape of the two phases. The additional energy required for the coexistence of phases is therefore not considered.

3.2. The second law of thermodynamics

To satisfy the thermodynamical consistency of the proposed model, we strive to fulfill the second law of thermodynamics in form of the Clausius–Duhem inequality

$$-\dot{\Psi} + \mathbf{S} \cdot \dot{\mathbf{E}} - \eta \dot{\theta} - \frac{1}{\theta} \mathbf{Q} \cdot \text{Grad } \theta \geq 0. \quad (7)$$

Here, \mathbf{S} is the second Piola–Kirchhoff stress tensor and \mathbf{Q} the referential heat flux vector. Assuming Fourier's law $\mathbf{Q} := -J_e \lambda_\theta \mathbf{C}^{-1} \text{Grad } \theta$ with the heat conductivity $\lambda_\theta > 0$, the heat conduction term $\mathbf{Q} \cdot \text{Grad } \theta / \theta$ is larger than or equal to zero.

Introducing the derived total free energy ((4)–(6) in (3)) and making use of (1) and (2) as well as of the property $\dot{\mathbf{E}} = \dot{\mathbf{C}}/2$, Eq. (7) results in

$$\begin{aligned} & \left(\mathbf{S} - 2 \mathbf{F}_t^{-1} \frac{\partial \Psi}{\partial \mathbf{C}_e} \mathbf{F}_t^{-T} \right) \cdot \frac{1}{2} \dot{\mathbf{C}} + \left(2 \mathbf{C}_e \frac{\partial \Psi}{\partial \mathbf{C}_e} - 2 \mathbf{F}_{te} \frac{\partial \Psi}{\partial \mathbf{C}_{te}} \mathbf{F}_{te}^T \right) \cdot \mathbf{d}_t \\ & + \left(2 \mathbf{C}_{te} \frac{\partial \Psi}{\partial \mathbf{C}_{te}} \right) \cdot \mathbf{d}_{td} - \frac{\partial \Psi}{\partial z} \dot{z} - \left(\frac{\partial \Psi}{\partial \theta} + \eta \right) \dot{\theta} \geq 0. \end{aligned} \quad (8)$$

This inequality implies sufficient conditions for the second Piola–Kirchhoff stress tensor \mathbf{S} and the entropy η per reference volume:

Table 1

Material parameters fitted to Helm and Haupt (2002).

| Parameter | Symbol | Value | Unit |
|------------------------------|-----------------|--------|-------------------|
| Lamé constant | λ | 29,190 | MPa |
| Shear modulus | μ | 15,037 | MPa |
| Kinematic hardening | μ_t | 14,000 | MPa |
| Limit of kinematic hardening | b | 700 | – |
| Energy difference | Δe_0 | –79.2 | MPa |
| Entropy difference | $\Delta \eta_0$ | –0.3 | MPa/K |
| Half height of hysteresis | k | 55 | MPa |
| Length of hysteresis | γ | 0.046 | – |
| Density | ρ_0 | 6400 | kg/m ³ |

$$\mathbf{S} = 2\mathbf{F}_t^{-1} \frac{\partial \Psi}{\partial \mathbf{C}_e} \mathbf{F}_t^{-\top}, \quad \eta = -\frac{\partial \Psi}{\partial \theta}. \quad (9)$$

Using the definitions

$$\mathbf{M} := 2\mathbf{C}_e \frac{\partial \Psi}{\partial \mathbf{C}_e}, \quad \mathbf{M}_t := 2\mathbf{C}_{te} \frac{\partial \Psi}{\partial \mathbf{C}_{te}} \quad \text{and} \quad \boldsymbol{\chi}_t := 2\mathbf{F}_{te} \frac{\partial \Psi}{\partial \mathbf{C}_{te}} \mathbf{F}_{te}^{\top} \quad (10)$$

the residual inequality reads

$$(\mathbf{M} - \boldsymbol{\chi}_t) \cdot \mathbf{d}_t + \mathbf{M}_t \cdot \mathbf{d}_{td} - \frac{\partial \Psi}{\partial z} \dot{z} \geq 0. \quad (11)$$

The stress tensors \mathbf{M} and \mathbf{M}_t are of so-called Mandel type. Clearly, \mathbf{M} is connected to the Kirchhoff stress tensor $\boldsymbol{\tau} = \mathbf{F}\mathbf{S}\mathbf{F}^{\top}$ by means of the relation $\mathbf{M} = \mathbf{F}_e^{\top} \boldsymbol{\tau} \mathbf{F}_e^{-\top}$. The structure of the tensor $\boldsymbol{\chi}_t$ is recognised to be analogous to the back stress tensor in kinematic hardening (Lion, 2000; Dettmer and Reese, 2004; Vladimirov et al., 2008). We will permit ourselves to use this notion also in the present context of phase transformations. \mathbf{M}_t and $\boldsymbol{\chi}_t$ are related to each other by the equation $\mathbf{M}_t = \mathbf{F}_{te}^{\top} \boldsymbol{\chi}_t \mathbf{F}_{te}^{-\top}$ which can be seen to be analogous to the previous one $\mathbf{M} = \mathbf{F}_e^{\top} \boldsymbol{\tau} \mathbf{F}_e^{-\top}$.

Due to the symmetry of $\partial \Psi / \partial \mathbf{C}_{te}$ the back stress tensor $\boldsymbol{\chi}_t$ is symmetric. This does not necessarily hold for the Mandel stress tensors \mathbf{M} and \mathbf{M}_t . However, in the special case where the free energy Ψ is additively decomposed into isotropic functions of \mathbf{C}_e and \mathbf{C}_{te} the coaxiality of \mathbf{C}_e and $\partial \Psi / \partial \mathbf{C}_e$ as well as of \mathbf{C}_{te} and $\partial \Psi / \partial \mathbf{C}_{te}$ implies the symmetry of \mathbf{M} and \mathbf{M}_t , respectively.

From the residual inequality (11) we can easily deduce evolution equations for \mathbf{d}_t and \mathbf{d}_{td} . Further, we have to find an evolution equation for z .

3.3. The three-phase mixture

In Eq. (4) we have introduced the martensitic volume fraction z to describe the ratio between martensitic and austenitic phases in the material. Obviously, such an average value defined in each material point (or Gauss point in the FE simulation) is not able to specify the micromechanical characteristics of shape memory alloys. Therefore, the mechanisms of nucleation and the growth of habit planes cannot be described in detail. The energy storage during the phase transformation can only be modelled approximately

by the second part (6) of the Helmholtz energy function. In spite of this fact, as already mentioned, most continuum mechanical models use only one scalar internal variable to describe the volume fractions of the phases since otherwise the FE implementation becomes rather elaborate and inefficient (see, e.g. Liang and Rogers (1992), Raniecki and Lexcellent (1994), Qidwai and Lagoudas (2000), Auricchio and Petrini (2004a) or Bouvet et al. (2004)).

In the present work the situation is more complex because we strive to cover pseudoelasticity and the shape memory effect by one model. For this reason at least two different martensite variants should be considered: on the one hand the unoriented martensite (z_u), also known as the martensite twins and on the other hand the oriented martensite (z_o). The unoriented martensite is a temperature induced martensite phase which develops during the cooling of the austenite below the martensite finish temperature M_f (see Fig. 1). The oriented martensite represents both the stress induced martensite occurring during the pseudoelastic phase transformation from austenite to martensite and the orientation of the martensite twins in pseudoplasticity. In this work we do not consider further martensite variants although the model could be enhanced accordingly. Both martensite variants are combined to the total martensitic volume fraction

$$z = z_u + z_o. \quad (12)$$

This additional split has already been proposed by, for example, Patoor et al. (1987), Brinson (1993), Leclercq and Lexcellent (1996) and Helm and Haupt (2003).

3.3.1. Pseudoelasticity

In the case of pseudoelasticity, we observe a phase transformation from austenite to oriented martensite and vice versa. The unoriented martensite is not present. Thus, the martensitic volume fraction z is only defined by dint of the oriented martensite fraction z_o ($z = z_o, z_u = 0$). The scalar value of z_o coincides with the norm of the transformation strain \mathbf{E}_t . It is assumed that the phase transformation from austenite to martensite as well as the orientation of the martensite twins do not initiate a volume change in the material. Raniecki et al. (1992) have shown that z_o can be expressed in terms of the von Mises norm of \mathbf{E}_t as well as the width of the hysteresis described by the parameter γ (see Fig. 2):

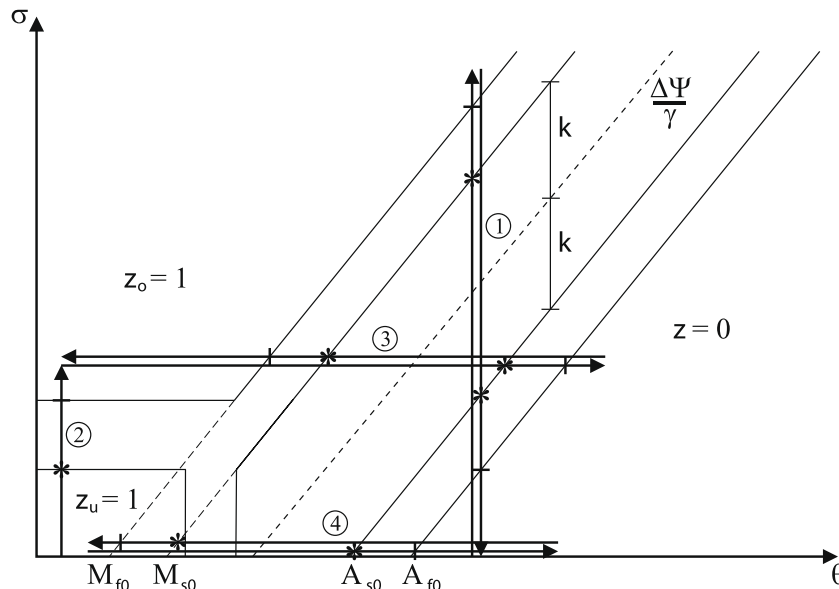


Fig. 1. Stress–temperature curve with regard to the 1D behaviour of SMA. The beginning of phase transformation is marked by *, the end by +. ① Pseudoelasticity; ② pseudoplasticity; ③ extrinsic two-way shape memory effect (induced via an external load) and ④ martensitic accommodation.

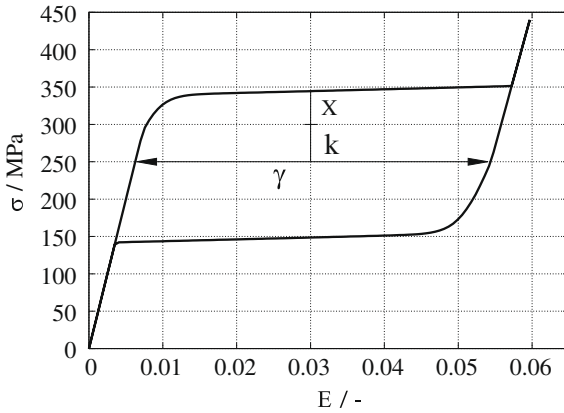


Fig. 2. 1D stress-strain hysteresis in pseudoelasticity.

$$z_o := \frac{\|\mathbf{E}_t\|}{\sqrt{\frac{3}{2}}\gamma} = \frac{\|\mathbf{E}_t\|}{\beta}. \quad (13)$$

Hence, the evolution of the oriented martensite

$$\dot{z}_o = \frac{1}{\beta} \frac{\mathbf{E}_t}{\|\mathbf{E}_t\|} \cdot \left(\frac{1}{2} \dot{\mathbf{C}}_t \right) = \frac{1}{\beta} \left(\mathbf{F}_t \frac{\mathbf{E}_t}{\|\mathbf{E}_t\|} \mathbf{F}_t^T \right) \cdot \mathbf{d}_t \quad (14)$$

depends on the evolution of the transformation strain $\dot{\mathbf{E}}_t = \dot{\mathbf{C}}_t/2$. In the absence of inelastic deformation the argument in the denominator $\|\mathbf{E}_t\|$ is zero, i.e. the function for \dot{z}_o is undefined. To overcome this problem we replace in this case the ratio $\mathbf{E}_t/\|\mathbf{E}_t\|$ by the deviatoric part of the total Green–Lagrange strain tensor $\mathbf{E}^D/\|\mathbf{E}^D\|$.

3.3.2. Pseudoplasticity

In the case of pseudoplasticity, the material is fully martensitic and therefore $z = 1$ and $\dot{z} = 0$ holds. However, due to the orientation of the martensite twins, the values of z_u and z_o can vary. Thus, we can conclude that z_u is also an implicit function of the transformation strain tensor \mathbf{E}_t :

$$z_u = z - z_o = 1 - \frac{\|\mathbf{E}_t\|}{\beta}. \quad (15)$$

For instance in the unloaded state, the material consists of unoriented martensite twins, so that $z_u = 1$ and $z_o = 0$ hold. During the loading and orientation of martensite twins the value of z_u decreases and concurrently, the value of z_o increases. The total martensite volume fraction though remains constant. So the evolution equation for the unoriented martensite during the orientation process is

$$\dot{z}_u = -\dot{z}_o = -\frac{1}{\beta} \left(\mathbf{F}_t \frac{\mathbf{E}_t}{\|\mathbf{E}_t\|} \mathbf{F}_t^T \right) \cdot \mathbf{d}_t. \quad (16)$$

3.3.3. Thermally driven phase transformation

The thermally driven phase transformation from austenite to self-accommodated martensite generally proceeds in a stress free state or at least below the stress level which initiates the orientation of martensite twins (see Fig. 1). Thus, no inelastic strain is generated during the phase transformation ($\mathbf{d}_t = \mathbf{0}$, $\mathbf{d}_{td} = \mathbf{0}$). As a result the oriented martensite which is in general given in terms of \mathbf{E}_t (see Eq. (13)) is zero ($z_o = 0$, $\dot{z}_o = 0$). Hence, in this case the evolution of the martensite volume fraction \dot{z}_u only depends on the evolution of the temperature $\dot{\theta}$. Additionally, according to Eq. (11) it correlates to the so-called driving force $\partial\Psi/\partial z$ which is abbreviated as $\Delta\Psi$ (see Fig. 1). The thermally driven phase transformation from austenite to martensite twins is described by

$$\dot{z}_u = \begin{cases} \frac{1}{2} \left(\frac{|\dot{\theta}| + \dot{\theta}}{A_{s0} - A_{f0}} \right) & \text{if } \theta \geq A_{s0}, \\ \frac{1}{2} \left(\frac{|\dot{\theta}| - \dot{\theta}}{M_{s0} - M_{f0}} \right) & \text{if } \theta \leq M_{s0}, \\ \dot{z}_u = 0 & \text{otherwise.} \end{cases} \quad (17)$$

Here, M_{f0} , M_{s0} , A_{s0} and A_{f0} are the phase transformation temperatures in the stress free state, respectively. This evolution equation covers both the phase transformation from martensite twins to austenite during heating ($\dot{\theta} > 0$) and the accommodation of martensite twins during cooling ($\dot{\theta} < 0$). The transformation path is signed as ④ in Fig. 1. Next, we take a look at the driving force $\Delta\Psi$. If we assume that most of the material parameters are equal in both phases ($\lambda^A = \lambda^M$, $\mu^A = \mu^M$, $\alpha_T^A = \alpha_T^M$, $c_d^A = c_d^M$), the driving force can be reduced to

$$\Delta\Psi = (e_0^M - e_0^A) - (\eta_0^M - \eta_0^A) \theta = \Delta e_0 - \Delta\eta_0 \theta. \quad (18)$$

Here, Δe_0 is the difference of internal energy and $\Delta\eta_0$ the difference of entropy between the austenite and the martensite phase. During the thermally driven phase transformation from twinned martensite to austenite, the martensitic volume fraction decreases ($\dot{z}_u < 0$). Hence, since the statement $\mathbf{d}_t = \mathbf{d}_{td} = \mathbf{0}$ holds, the driving force has to be positive to fulfill the remaining inequality

$$-\underbrace{\frac{\partial\Psi}{\partial z}}_{\Delta\Psi} \dot{z}_u \leq 0. \quad (19)$$

Accordingly, the driving force must be negative when cooling the material from austenite to twinned martensite ($\dot{z}_u > 0$). The restrictions on $\Delta\Psi$ can be reformulated to read

$$\Delta e_0 - \Delta\eta_0 A_{s0} \geq 0, \quad \Delta e_0 - \Delta\eta_0 M_{s0} \leq 0. \quad (20)$$

Dividing both equations by $\Delta\eta_0$ leads for $\Delta\eta_0 > 0$ to the statements $(\Delta e_0/\Delta\eta_0) \geq A_{s0}$ and $(\Delta e_0/\Delta\eta_0) \leq M_{s0}$ which contradict each other. On the other hand, choosing $\Delta\eta_0 < 0$ yields $M_{s0} \leq (\Delta e_0/\Delta\eta_0) \leq A_{s0}$. Since the temperatures M_{s0} and A_{s0} are positive, the parameter Δe_0 must also be negative.

Explicit expressions for Δe_0 and $\Delta\eta_0$ can be derived by means of the stress-temperature diagram in Fig. 2. Here, the function $\Delta\Psi/\gamma = (\Delta e_0 - \Delta\eta_0 \theta)/\gamma$ is given by a dotted line (note that in 1D the function $\beta = \sqrt{3/2}\gamma$ reduces to $\beta = \gamma$). The distance between this line and the equivalent transformation temperatures (M_s and A_s) is constant. The distance in the direction of the stress axis is equal to the material parameter k . By using the phase transformation temperatures M_{s0} and A_{s0} (the index 0 stands for the phase transformation at zero stress) both material parameters Δe_0 and $\Delta\eta_0$ are given as

$$\Delta e_0 = \gamma k \frac{M_{s0} + A_{s0}}{M_{s0} - A_{s0}} \quad \text{and} \quad \Delta\eta_0 = \gamma k \frac{2}{M_{s0} - A_{s0}} \quad (21)$$

resulting in $\Delta e_0/\Delta\eta_0 = (M_{s0} + A_{s0})/2$. Thus, the condition $M_s \leq (\Delta e_0/\Delta\eta_0) \leq A_s$ is fulfilled.

3.4. The phase transformation function

The previous definition of the martensitic volume fraction z allows us to specify the Clausius–Duhem inequality (11) for various cases.

3.4.1. Pseudoelasticity

The first case is the transformation from austenite to oriented martensite and vice versa, i.e. the effect of pseudoelasticity. Here, the martensite volume fraction z and its time derivative \dot{z} are expressed by the transformation strain \mathbf{E}_t and its time derivative $\dot{\mathbf{E}}_t$ ((13) and (14)). This correlation can be inserted into the Clausius–Duhem inequality (11)

$$\left(\mathbf{M} - \chi_t - \frac{\Delta\Psi}{\beta} \mathbf{F}_t \frac{\mathbf{E}_t}{\|\mathbf{E}_t\|} \mathbf{F}_t^T \right) \cdot \mathbf{d}_t + \mathbf{M}_t \cdot \mathbf{d}_{td} \geq 0. \quad (22)$$

3.4.2. Pseudoplasticity

During the orientation of the martensite twins the total martensitic volume fraction z remains 1 and therefore $\dot{z} = 0$ holds. Consequently, we obtain from (11) the inequality

$$(\mathbf{M} - \chi_t) \cdot \mathbf{d}_t + \mathbf{M}_t \cdot \mathbf{d}_{td} \geq 0. \quad (23)$$

3.4.3. Thermally driven phase transformation

The thermally driven phase transformation leads, as already discussed in Section 3.3, to the requirement $-\Delta\Psi \dot{z} \geq 0$ which is fulfilled by the evolution (17) and the correct choice of Δe_0 and $\Delta\eta_0$.

The cases pseudoelasticity and pseudoplasticity discussed in the first part of this section can be easily summarised if we consider the fact that pseudoelasticity takes place above the austenite start temperature A_s . In this temperature range the driving force $\Delta\Psi$ is positive. If we replace $\Delta\Psi$ in (22) by $\langle\Delta\Psi\rangle := (|\Delta\Psi| + \Delta\Psi)/2$ the following inequality

$$\left(\mathbf{M} - \chi_t - \underbrace{\frac{\langle\Delta\Psi\rangle}{\beta} \mathbf{F}_t \frac{\mathbf{E}_t}{\|\mathbf{E}_t\|} \mathbf{F}_t^T}_{\chi_z} \right) \cdot \mathbf{d}_t + \mathbf{M}_t \cdot \mathbf{d}_{td} \geq 0, \quad (24)$$

covers both, pseudoelasticity and pseudoplasticity. Using (24) and considering the fact that the phase transformation proceeds without any volume change, the symmetric part of the deformation rate tensor \mathbf{d}_t is in correlation with the deviatoric parts of the Mandel stress \mathbf{M}^D and the back stress $\chi^D = \chi_t^D + \chi_z^D$. The second tensor \mathbf{d}_{td} correlates with the deviatoric part of the Mandel stress \mathbf{M}_t^D . Finally, in case of the temperature induced martensite transformation the strain rate tends to be zero. Thus, we only have to fulfill the evolution equation for \dot{z}_u (17).

To define the initiation of the phase transformation, we introduce a phase transformation criterion similar to the common theory of plasticity. Due to the fact that shape memory alloys can exhibit a distinct tension–compression asymmetry (e.g. Kakeshita et al., 1992; Liu et al., 1998; Lim and McDowell, 1999; Gall and Sehitoglu, 1999; Raniecki et al., 2001; Aleong et al., 2002), we introduce a Prager–Lode function as the phase transformation criteria (see, e.g. Freudenthal and Gou, 1969; Auricchio and Petrini, 2004b)

$$\Phi_{PL} = \|\mathbf{T}^D\| + m \frac{2 \operatorname{tr}((\mathbf{T}^D)^3)}{3 \operatorname{tr}((\mathbf{T}^D)^2)} - \sqrt{\frac{2}{3}} k, \quad (25)$$

where k is a material parameter defining the half height of the hysteresis (see Fig. 2). The tensor $\mathbf{T}^D = \mathbf{M}^D - \chi^D$ is the deviatoric part of the effective stress. The term in the denominator $\operatorname{tr}((\mathbf{T}^D)^2)/2$ is the second invariant and the one in the numerator $\operatorname{tr}((\mathbf{T}^D)^3)/3$ the third invariant of the deviatoric stress \mathbf{T}^D , respectively. The second invariant of a deviatoric tensor is in any case positive whereas the third invariant, i.e. the determinant of the deviatoric tensor, can be positive or negative for $\mathbf{T}^D \neq \mathbf{0}$. The material parameter m controls the influence of the additional term. When choosing a positive value for m ($0 < m \leq (3/8)\sqrt{(3/2)}$) the elastic domain will be shifted towards compression (see Fig. 3). The shift of the onset has been experimentally investigated by, for example, Lexcellent et al. (2002) who have carefully evaluated biaxial loading paths on polycrystalline Cu–Al based shape memory alloys. Their results yield a similar phase transformation function as in Eq. (25) (see also Vieille et al. (2007)). The limitation $m \leq (3/8)\sqrt{(3/2)}$ is necessary to assure the convexity of the phase transformation function. See for more details the recent work of Raniecki and Mroz (2008).

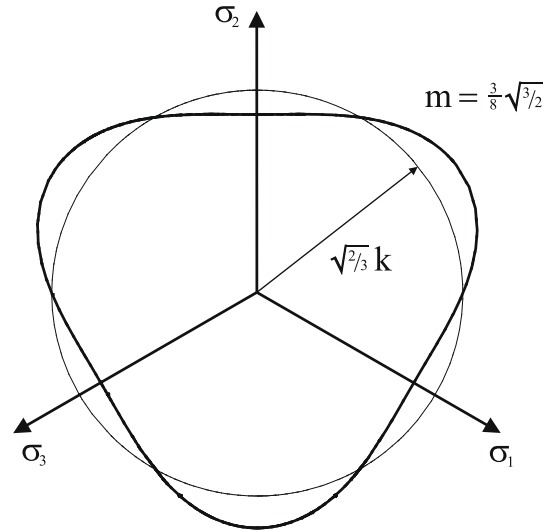


Fig. 3. The surface of the phase transformation function in the 3D stress space. Thin line: von Mises phase transformation ($m=0$); thick line: Prager–Lode phase transformation ($m = \frac{3}{8}\sqrt{\frac{3}{2}}$).

Now, with regard to the phase transformation criterion (25) we choose an adequate evolution equation for \mathbf{d}_t by using the normality rule

$$\mathbf{d}_t = \dot{\lambda} \frac{\partial \Phi}{\partial \mathbf{M}}. \quad (26)$$

To determine \mathbf{d}_{td} we introduce an evolution equation which is similar to the function proposed by Armstrong and Frederick (1966) for kinematic hardening and has already been used by Helm and Haupt (2003):

$$\mathbf{d}_{td} = \dot{\lambda} \frac{b}{\mu_t} \mathbf{M}_t^D. \quad (27)$$

Here, b is a further material parameter which controls the saturation of the storage during the phase transformation. In both equations, (26) and (27), $\dot{\lambda}$ is the transformation multiplier which correlates to the phase transformation criterion Φ via the Kuhn–Tucker conditions

$$\dot{\lambda} \geq 0, \quad \Phi \leq 0 \quad \text{and} \quad \dot{\lambda} \Phi = 0. \quad (28)$$

4. Thermomechanical coupling

The heat conduction equation postulates the conservation of energy and states that mechanical energy can be transformed into thermal energy and vice versa. In the reference configuration the balance of internal energy (first law of thermodynamics) is defined as

$$\operatorname{Div} \mathbf{Q} + \dot{e} = \frac{1}{2} \mathbf{S} \cdot \dot{\mathbf{C}} + r_0. \quad (29)$$

Here, r_0 is the external heat source which is neglected in the following ($r_0 = 0$). Using the Legendre transformation $e = \Psi + \eta \theta$ the time derivative of the internal energy can be replaced by $\dot{e} = \dot{\Psi} + \dot{\eta} \theta + \eta \dot{\theta}$. We introduce the latter equation into (29) and as in Eq. (8), we make use of (3) leading to

$$\begin{aligned} \operatorname{Div} \mathbf{Q} + \frac{\partial \Psi}{\partial \mathbf{C}_e} \cdot \dot{\mathbf{C}}_e + \frac{\partial \Psi}{\partial \mathbf{C}_{te}} \cdot \dot{\mathbf{C}}_{te} + \frac{\partial \Psi}{\partial z} \dot{z} \\ - \left(\frac{\partial^2 \Psi}{\partial \theta^2} \dot{\theta} + \frac{\partial^2 \Psi}{\partial \theta \partial \mathbf{C}_e} \cdot \dot{\mathbf{C}}_e + \frac{\partial^2 \Psi}{\partial \theta \partial \mathbf{C}_{te}} \cdot \dot{\mathbf{C}}_{te} + \frac{\partial^2 \Psi}{\partial \theta \partial z} \dot{z} \right) \theta = \frac{1}{2} \mathbf{S} \cdot \dot{\mathbf{C}}. \end{aligned} \quad (30)$$

We insert Eqs. (1) and (2) into (30). Subsequently we use Eqs. (9), (10)₁, (10)₂ and (10)₃ for the second Piola–Kirchhoff stress tensor \mathbf{S} , the Mandel stress tensors \mathbf{M} and \mathbf{M}_t as well as for the back stress tensor χ_t , respectively, which yields together with $\Delta\Psi = \Delta e_0 - \Delta\eta_0\theta$ and $\partial(\Delta\Psi)/\partial\theta = -\Delta\eta_0$ the equation

$$c_d \dot{\theta} = \underbrace{\left(\mathbf{M} - \theta \frac{\partial \mathbf{M}}{\partial \theta} - \chi_t \right) \cdot \mathbf{d}_t + \mathbf{M}_t \cdot \mathbf{d}_{t_d} - \Delta e_0 \dot{z}}_{w_{int}} + \underbrace{\theta \frac{\partial \mathbf{S}}{\partial \theta} \cdot \dot{\mathbf{C}} - \text{Div} \mathbf{Q}}_{w_{ext}}. \quad (31)$$

The evolution of temperature depends on three, partially combined terms. The first term w_{int} is called internal stress power and represents the energy dissipation due to the evolution of the internal variables. Splitting the Helmholtz free energy $\Psi = e - \theta\eta$ into energetic (e) and entropic ($-\theta\eta$) parts it can be shown that $\mathbf{M} - \theta(\partial\mathbf{M}/\partial\theta)$ is the energetic part of \mathbf{M} given by $2\mathbf{C}_e(\partial e/\partial\mathbf{C}_e)$. The tensors χ_t and \mathbf{M}_t are already of purely energetic character because Ψ_t does not have an entropic contribution. Δe_0 is obviously the energetic part of $\Delta\Psi$. Thus, w_{int} includes only energetic contributions. In contrast, the second term w_{ext} contains the entropic part of the second Piola–Kirchhoff stress tensor coupled to the external deformation rate $\dot{\mathbf{C}}$. In case of very slow or quasistatic loading conditions w_{ext} tends to zero and can be neglected. The third term includes the heat flux vector \mathbf{Q} . As already mentioned before, the heat flux can be defined via Fourier's law. The rate \dot{z} is defined by the evolution equations discussed in Section 3.3.

5. Numerical implementation

5.1. Final form of the evolution equations

Up to this point, the evolution equations (26) and (27) are formulated in the intermediate configuration. To derive an efficient scheme for time integration we pull them back to the reference configuration:

$$\dot{\mathbf{C}}_t = 2\dot{\lambda} \mathbf{F}_t^T \frac{\partial \Phi}{\partial \mathbf{M}} \mathbf{F}_t = 2\dot{\lambda} \mathbf{N}_Y \mathbf{C}_t, \quad (32)$$

$$\dot{\mathbf{C}}_{t_d} = 2\dot{\lambda} \frac{b}{\mu_t} \mathbf{F}_{t_d}^T \mathbf{M}_t^D \mathbf{F}_{t_d} = 2\dot{\lambda} \frac{b}{\mu_t} (\mathbf{Y}_t^D \mathbf{C}_{t_d}). \quad (33)$$

The tensors \mathbf{Y}_t and \mathbf{N}_Y were already derived in detail in Reese and Christ (2008) wherein the above mentioned relations $\mathbf{F}_t^T \frac{\partial \Phi}{\partial \mathbf{M}} \mathbf{F}_t = \mathbf{N}_Y \mathbf{C}_t$ and $\mathbf{F}_{t_d}^T \mathbf{M}_t^D \mathbf{F}_{t_d} = \mathbf{Y}_t^D \mathbf{C}_{t_d}$ has been thoroughly proved. An important aspect of (32) and (33) is that the rates $\dot{\mathbf{C}}_t$ and $\dot{\mathbf{C}}_{t_d}$ can be expressed as functions of \mathbf{C} , \mathbf{C}_t and \mathbf{C}_{t_d} . Thus, \mathbf{C}_t and \mathbf{C}_{t_d} play the role of internal variables. The final integration algorithm does not change with respect to the one presented in Reese and Christ (2008), so that the following equations have to be solved at the material level:

$$\begin{aligned} \mathbf{R}_1 &= -\mathbf{C}_{t_n}^{-1} + \mathbf{U}_t^{-1} \exp(\dot{\lambda} \Delta t \mathbf{U}_t^{-1} \mathbf{f} \mathbf{U}_t^{-1}) \mathbf{U}_t^{-1} = \mathbf{0}, \\ \mathbf{R}_2 &= -\mathbf{C}_{t_d n}^{-1} + \mathbf{U}_{t_d}^{-1} \exp(\dot{\lambda} \Delta t \mathbf{U}_{t_d}^{-1} \mathbf{f}_t \mathbf{U}_{t_d}^{-1}) \mathbf{U}_{t_d}^{-1} = \mathbf{0}, \\ \mathbf{R}_3 &= \Phi = 0. \end{aligned} \quad (34)$$

Here, $\mathbf{U}_t = \sqrt{\mathbf{C}_t}$ and $\mathbf{U}_{t_d} = \sqrt{\mathbf{C}_{t_d}}$ are the respective stretch tensors. We further introduce the functions $\mathbf{f} = 2\mathbf{N}_Y \mathbf{C}_t$ and $\mathbf{f}_t = b/\mu_t (\mathbf{Y}_t^D \mathbf{C}_{t_d})$. One important aspect is that the algorithm exactly preserves the required plastic incompressibility for the evolution equations. The scheme is based on the exponential map given in closed form. No further approximation is necessary. Using Voigt notation the symmetric tensors \mathbf{R}_1 and \mathbf{R}_2 can be represented as six-dimensional vectors. The equation system (34) finally consists of 13 scalar equations for the six-dimensional Voigt notations of \mathbf{C}_t and \mathbf{C}_{t_d} as well as the discrete transformation multiplier $\dot{\lambda} = \dot{\lambda} \Delta t$.

5.2. Thermomechanical algorithm

The numerical solution of the coupled thermomechanical boundary value problem can be approached either by monolithic or by staggered time-stepping algorithms. When a consistent linearisation is performed, the monolithic approach, where the two balance equations for linear momentum and internal energy are solved simultaneously, leads to a larger system of equations with a non-symmetric stiffness matrix. Staggered schemes uncouple the problem into two smaller, symmetric problems which are solved one after another. Such an approach also offers the possibility to employ different time scales for the thermal and the mechanical part. However, using the staggered approach unconditional stability cannot be guaranteed if the common isothermal split is used (Simo and Miehe, 1992; Armero and Simo, 1993). Further it is important to mention that in our case already the purely mechanical problem is not symmetric. Hence, the benefit of using staggered time-stepping is in the present situation not very high, so that we apply the monolithic approach. Note that in the following, quantities written in Voigt notation are indicated by italic bold letters.

The semidiscrete boundary value problem depends on the global variables \mathbf{V}_M (the nodal displacements), \mathbf{V}_T (the nodal temperatures) and on the respective time derivatives $\dot{\mathbf{V}}_M$ and $\dot{\mathbf{V}}_T$. It can be written as

$$\mathbf{R}_M(\mathbf{V}_M, \mathbf{V}_T) = \mathbf{P}_M(t), \quad (35)$$

$$\mathbf{R}_T(\mathbf{V}_M, \dot{\mathbf{V}}_M, \mathbf{V}_T, \dot{\mathbf{V}}_T) = \mathbf{P}_T(t). \quad (36)$$

Here, the indices M and T characterise the mechanical and the thermal phase, respectively. The above differential equation system is of first order and can be solved via classical time integration algorithms, e.g. the backward Euler scheme:

$$\mathbf{R}_M(\mathbf{V}_{Mn+1}, \mathbf{V}_{Tn+1}) = \mathbf{P}_M(t_{n+1}), \quad (37)$$

$$\mathbf{R}_T(\mathbf{V}_{Mn+1}, \dot{\mathbf{V}}_{Mn+1}, \mathbf{V}_{Tn+1}, \dot{\mathbf{V}}_{Tn+1}) = \mathbf{P}_T(t_{n+1}), \quad (38)$$

where the time derivatives are computed as

$$\dot{\mathbf{V}}_{Mn+1} = \frac{1}{\Delta t} (\mathbf{V}_{Mn+1} - \mathbf{V}_{Mn}) \quad \dot{\mathbf{V}}_{Tn+1} = \frac{1}{\Delta t} (\mathbf{V}_{Tn+1} - \mathbf{V}_{Tn}). \quad (39)$$

Hence, Eqs. (37) and (38) only depend on the global variables \mathbf{V}_M and \mathbf{V}_T . The linearisation of the boundary value problem via the Newton method requires the computation of the consistent tangents

$$\begin{aligned} \mathbf{K}_{MM} &= \frac{\partial \mathbf{R}_M}{\partial \mathbf{V}_{Mn+1}}, \quad \mathbf{K}_{MT} = \frac{\partial \mathbf{R}_M}{\partial \mathbf{V}_{Tn+1}}, \\ \mathbf{K}_{TM} &= \frac{\partial \mathbf{R}_T}{\partial \mathbf{V}_{Mn+1}} \quad \text{and} \quad \mathbf{K}_{TT} = \frac{\partial \mathbf{R}_T}{\partial \mathbf{V}_{Tn+1}}. \end{aligned} \quad (40)$$

With the following abbreviations

$$\begin{aligned} \mathbf{K} &:= \begin{bmatrix} \mathbf{K}_{MM} & \mathbf{K}_{MT} \\ \mathbf{K}_{TM} & \mathbf{K}_{TT} \end{bmatrix}, \quad \mathbf{V}^T := [\mathbf{V}_M^T \quad \mathbf{V}_T^T], \\ \mathbf{P}^T &:= [\mathbf{P}_M^T \quad \mathbf{P}_T^T] \quad \text{and} \quad \mathbf{R}^T := [\mathbf{R}_M^T \quad \mathbf{R}_T^T] \end{aligned} \quad (41)$$

the iteration algorithm of the nonlinear equation system (37) and (38) reads

$$\begin{aligned} \mathbf{K}_i \Delta \mathbf{V}_{i+1} &= \mathbf{P} - \mathbf{R}_i := -\mathbf{G}_i \\ \mathbf{V}_{i+1} &= \mathbf{V}_i + \Delta \mathbf{V}_{i+1} \\ i &\leftarrow i + 1 \quad \text{until} \quad \|\mathbf{G}_i\| \leq \text{tol} \end{aligned} \quad (42)$$

Here, the index $n+1$ was neglected.

The Newton iteration includes the linearisation of the second Piola–Kirchhoff stress $\mathbf{S} = \hat{\mathbf{S}}(\mathbf{C}, \theta, \mathbf{C}_t)$, the internal stress power

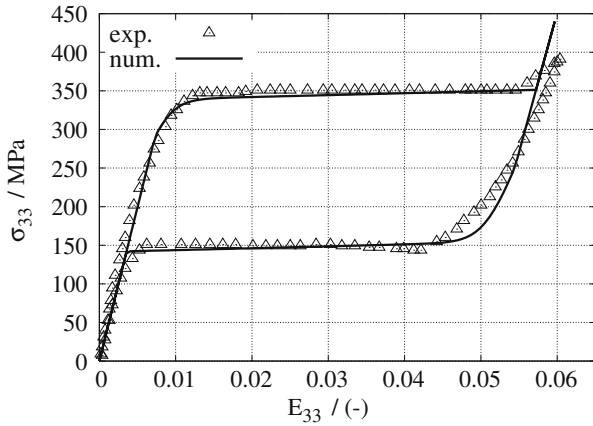


Fig. 4. Fitting of the material parameters at a pseudoelastic tension test.

$w_{\text{int}} = \hat{w}_{\text{int}}(\mathbf{C}, \theta, \mathbf{C}_t, \mathbf{C}_{t_d})$ and the external stress power $w_{\text{ext}} = \hat{w}_{\text{ext}}(\mathbf{C}, \theta, \mathbf{C}_t)$ with respect to a prescribed deformation and temperature, respectively.

6. Numerical examples

6.1. Thermomechanical couplings

In this section we concentrate on the investigation of the influence of the thermomechanical coupling in the material model. The mechanical parameters are fitted to an experimental tension test by Helm and Haupt (2002) (see Fig. 4) and are listed in Table 1. Additionally, we introduce common values for the thermal material parameters of NiTi, $\lambda_\theta = 18.0 \text{ W/(m K)}$, $c_d = 2.944 \text{ MPa/K}$ and $\alpha_T = 1.06 \times 10^{-5} / \text{K}$ (see, e.g. Van Humbeeck (2001) or Eaton-Evans et al. (2006)). We confine ourselves to adiabatic boundary conditions, i.e. there is no heat transfer between the sample and the surroundings. The tests are carried out at a long, thin strip ($l = 100 \text{ mm}$, $b = 12 \text{ mm}$ and $t = 4 \text{ mm}$, see Fig. 5). The reason for choosing such a longish geometry is to avoid a strong mutual

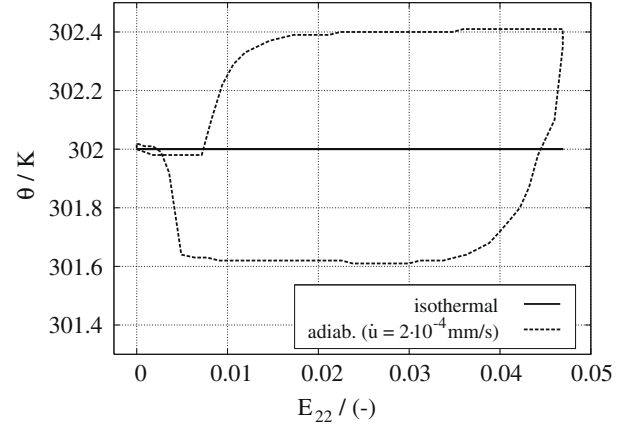


Fig. 6. Temperature evolution during the isothermal and the adiabatic loading process.

influence of the thermal boundary conditions at both ends and the heat evolution in the middle of the sample. By utilizing the symmetry of the sample, the strip can be reduced to a fourth of its original dimension.

6.1.1. Pseudoelasticity

In the first example we investigate the difference between the thermomechanically coupled and uncoupled loading condition in case of pseudoelasticity. The strip is fixed at both ends and will be elongated until a given displacement $u_0 = 2.0 \text{ mm}$ (see Fig. 5a). The displacement u_0 is applied in 10,000 s ($\dot{u}_0 = 2.0 \times 10^{-4} \text{ mm/s}$), which is comparable to a quasistatic process. The initial temperature θ_0 is equal to 302 K. In the uncoupled problem, isothermal conditions are considered so that the temperature θ_0 remains constant. In the coupled problem, only the temperature at the fixed end of the strip is set to θ_0 whereas in the other nodes the temperature can evolve depending on the loading history. The temperature–strain diagram (Fig. 6), the stress–strain diagram (Fig. 7) and the martensitic volume fraction–strain diagram (Fig. 8) are evaluated at point P in the middle of the sample (see

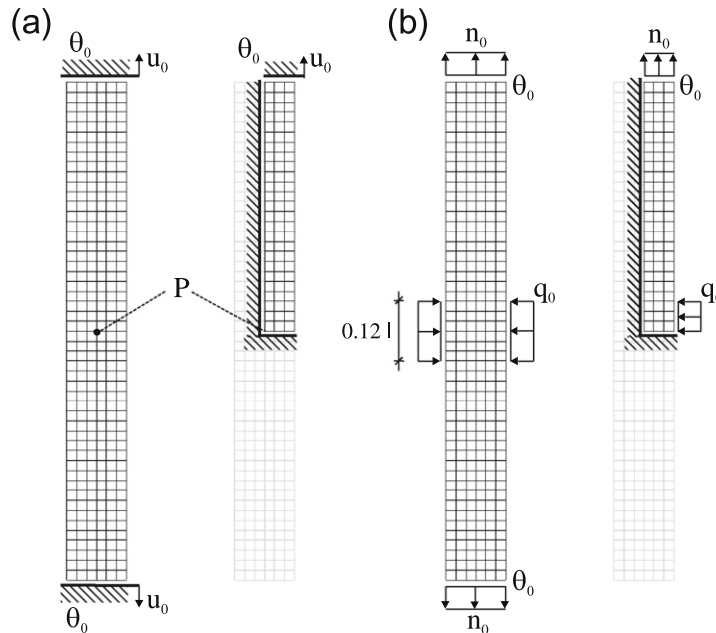


Fig. 5. FE discretisation and boundary conditions of the long strip to simulate (a) pseudoelasticity and (b) the shape memory effect.

Fig. 5). As expected, the temperature in the uncoupled problem (Fig. 6) remains constant. In case of the coupled problem, the temperature increases during the phase transformation from austenite to martensite and decreases during the phase transformation of the martensite back to austenite. However, the maximum temperature difference of $\Delta\theta = 0.4$ K does not significantly affect the development of the stress–strain hysteresis (Fig. 7) and the evolution of the martensitic volume fraction z (Fig. 8). This is due to the fact that for quasistatic loading we compute the stationary thermomechanical state which is characterised for the present choice of boundary conditions by a homogeneous temperature field. So, the results of the thermomechanical problem for quasistatic loading come close to the results of an isothermal, uncoupled problem.

Next, the time in which the loading is applied is decreased from 10,000 s ($\dot{u}_0 = 2.0 \times 10^{-4}$ mm/s) to 1000 s ($\dot{u}_0 = 2.0 \times 10^{-3}$ mm/s) and to 100 s ($\dot{u}_0 = 2.0 \times 10^{-2}$ mm/s). The temperature boundary conditions are the same as before. When the maximum displacement is reached ($u_{max} = 2.0$ mm) it is held constant for 10 s before unloading. Due to the increased loading rate \dot{u}_0 , the evolution of temperature during the loading history changes considerably (Fig. 9). The temperature difference during the phase transformation rises to $\Delta\theta = 4$ K (at $\dot{u}_0 = 2.0 \times 10^{-3}$ mm/s) and $\Delta\theta = 21$ K (at $\dot{u}_0 = 2.0 \times 10^{-2}$ mm/s), respectively. The loading break of 10 s at u_{max} yields a decrease of the temperature due to the diffusion of heat to the surrounding material. We also observe a relaxation of the stress similar to viscoelastic behaviour. If the loading break

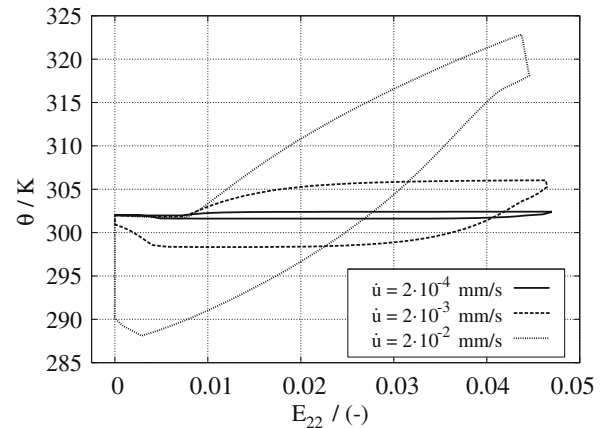


Fig. 9. Temperature evolution during different adiabatic loading processes.

is prolonged, the temperature decreases to the maximum value of the quasistatic analysis ($\Delta\theta = 0.4$ K). After complete unloading the temperature still differs from the initial temperature $\theta_0 = 302$ K. A second loading break is necessary to reach the initial temperature (at $\dot{u}_0 = 2.0 \times 10^{-3}$ mm/s: 10 s and at $\dot{u}_0 = 2.0 \times 10^{-2}$ mm/s: 20 s). The rise of the heat production by increasing \dot{u}_0 also affects the stress (Fig. 10) and the martensitic volume fraction (Fig. 11). The stress increases during the phase transformation from austenite to martensite up to 530 MPa (at $\dot{u}_0 = 2.0 \times 10^{-2}$ mm/s), i.e. to a 150 MPa higher value than for the quasistatic process. The reason

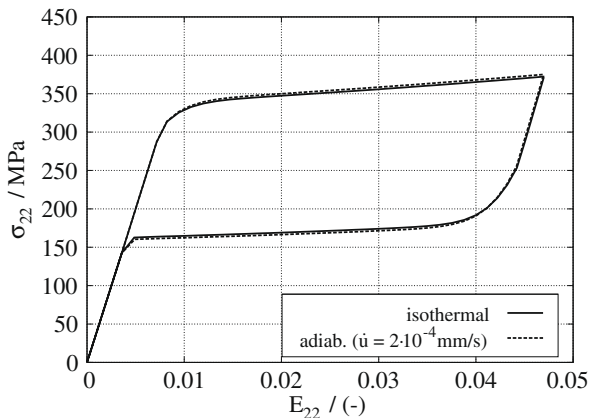


Fig. 7. Stress evolution during the isothermal and the adiabatic loading process.

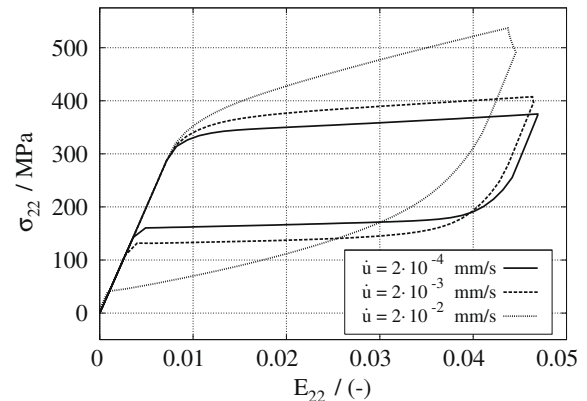


Fig. 10. Stress evolution during different adiabatic loading processes.

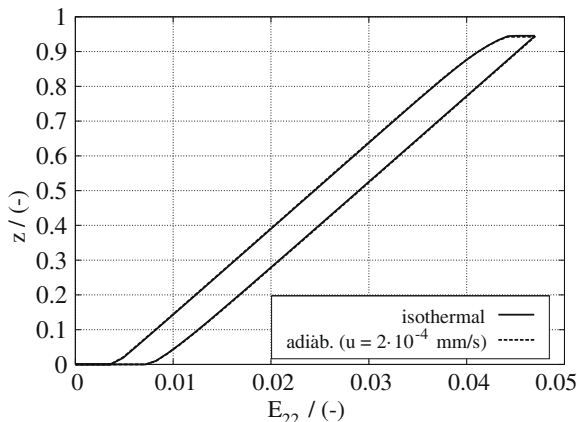


Fig. 8. Evolution of martensitic volume fraction during the isothermal and the adiabatic loading process.

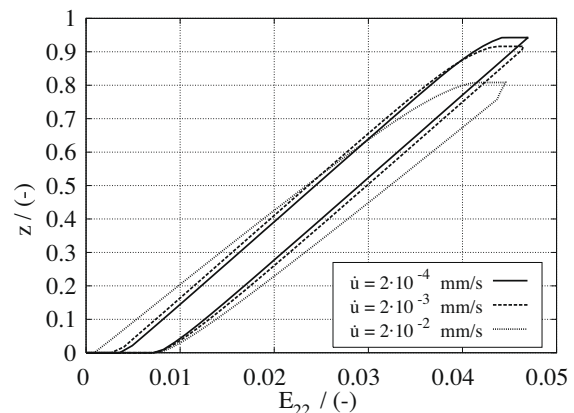


Fig. 11. Evolution of the martensitic volume fraction during different adiabatic loading processes.

for this is that the temperature rises very fast as a result of the higher loading rate. The heat does not have enough time to diffuse. Consequently, a local temperature peak develops which causes an increase of the upper stress plateau for the phase transformation. As in the temperature evolution, the load break at u_{max} leads to a decrease of the stress plateau (see Fig. 12a). In unloading the same phenomenon can be observed. The temperature falls very fast and the driving force decreases. At the end of the phase transformation from martensite to austenite, the stress value is only about 40 MPa. The previously described observations obtained by the numerical modelling are confirmed by experimental results (e.g. Leo et al. (1993), Entermeier et al. (2000), Matsuzaki et al. (2001) or Pieczyska et al. (2006)).

6.1.2. Free shape memory effect

After the investigation of the thermomechanical coupling in pseudoelasticity, we now concentrate on the shape memory effect. Again we investigate the long strip but the boundary conditions are modified (see Fig. 5b). We apply a distributed load $n_0 = 150 \text{ N/mm}^2$ and a given temperature $\theta_0 = 225 \text{ K}$ at the ends of the strip. The initial temperature θ_0 is set below the martensite finish temperature ($M_f = 235 \text{ K}$). Thus, the sample completely consists of unoriented martensite at the beginning ($z_u = 1$). Here, the load n_0 is applied in a quasistatic process ($\dot{n}_0 = 150 \times 10^{-4} \text{ N/(mm}^2 \text{ s)}$). After the loading–unloading cycle the load n_0 is removed and the sample is heated by an heat flux $q_0 = 200 \text{ kJ}$ in the middle. Here, the time in which the heat flux is applied varies between $10,000 \text{ s}$ ($\dot{q}_0 = 200 \times 10^{-4} \text{ kJ/s}$), 1000 s ($\dot{q}_0 = 200 \times 10^{-3} \text{ kJ/s}$) and 100 s ($\dot{q}_0 = 200 \times 10^{-2} \text{ kJ/s}$). The results are again taken from node P . In Fig. 13 the stress–strain relation upon the loading–unloading cycle is visualised. During loading path ①, a part of the unoriented martensite (described by z_u) turns to oriented martensite (see Fig. 15). After unloading (loading path ②) the strip has recovered from elastic strain and is again free of stress. However, the oriented martensitic state involves permanent strain which can only be restored by a heating process to follow. Applying the heat flux q_0 after the loading–unloading cycle (① and ②), loading path ③ results in an increase of temperature (see Fig. 14). At the beginning the thermoelastic effect, originating from the term w_{ext} in (31), yields a slight increase of strain. Then, at $\theta = 263 \text{ K}$

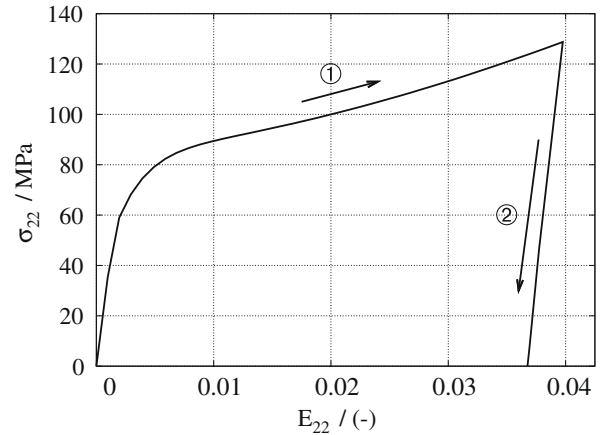


Fig. 13. Stress–strain diagram of the loading cycle (①: loading, ②: unloading).

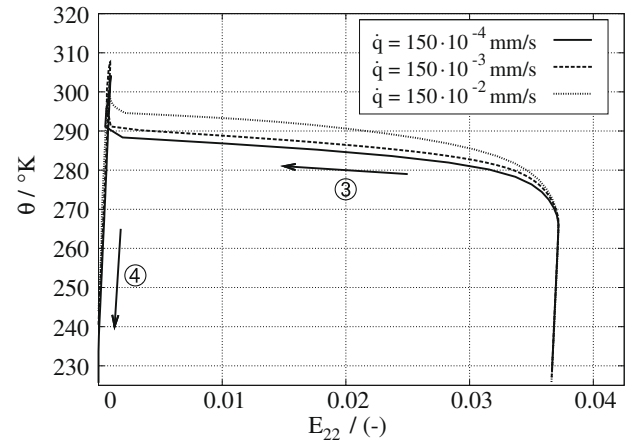


Fig. 14. Temperature–strain diagram of the heating cycle (③: heating, ④: cooling).

the austenite start temperature A_s is reached and the phase transformation of the partially oriented martensite to austenite is initi-

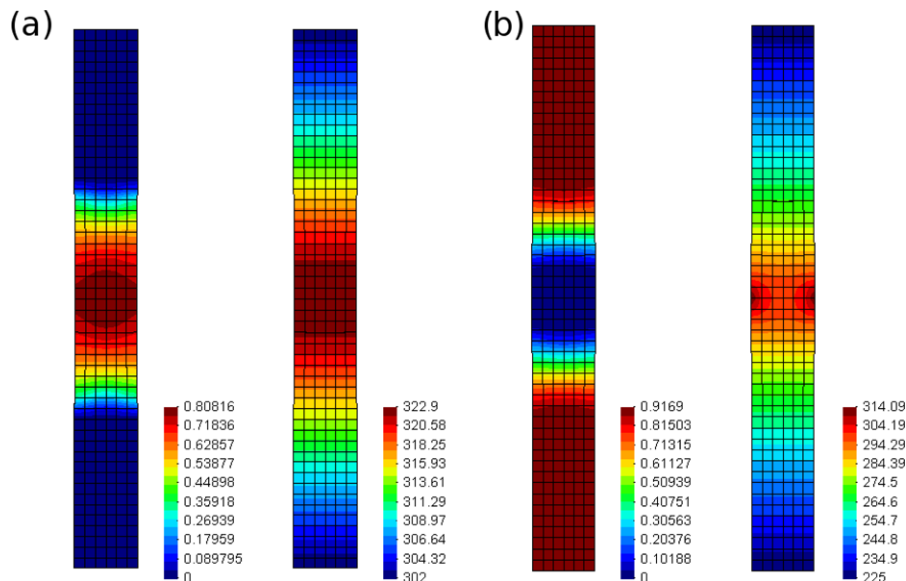


Fig. 12. Distribution of martensitic volume fraction (left) and temperature (right, in K) in case of (a) pseudoelasticity (at the end of loading) and (b) the shape memory effect (at the end of heating).

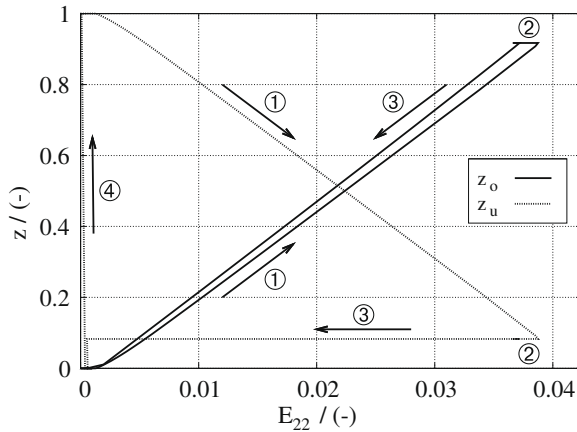


Fig. 15. Martensitic volume fraction–strain diagram of the complete loading history (①: loading, ②: unloading, ③: heating, ④: cooling).

ated. By increasing \dot{q}_0 the end of the phase transformation is shifted because of the accompanied increase of the austenite finish temperature A_f . However, the variation of \dot{q}_0 affects the material behaviour less than \dot{u}_0 in the previous example (Fig. 10). The heat flux q_0 leads to a temperature rise up to approximately 308 K. In all three cases the end of the phase transformation is reached (Fig. 12b). In (Fig. 12b) conjunction with the phase transformation the permanent strain is finally recovered and the strip returns to its initial shape. When the sample is cooled down ④ the temperature falls below the martensite start temperature $M_s = 250$ K and the austenite reforms to the unoriented martensite.

6.1.3. Suppressed shape memory effect

In practice the shape memory effect is frequently used in actuators or locking units (see, e.g. Xu et al., 1999; Hesse et al., 2004). Here, the free recovery of strain is mostly suppressed by a constraint or contact to other outer components. The contact and the associated suppression of strain recovery during heating yields an increase of internal stress in the shape memory alloy which is able to produce a high contact force. The value of the force can then be controlled by the supplied amount of heat. To simulate the suppressed shape memory effect we slightly change the boundary conditions from the previous example. The strip is loaded and unloaded by $n_0 = 150$ N/mm² as before. However, before applying the heat flux $q_0 = 250$ kJ, we fix the end of the strip so that the residual strain due to oriented martensite cannot be recovered. Since \dot{q}_0 does not affect the material response significantly, we only work with $\dot{q}_0 = 250 \times 10^{-4}$ kJ/s. Figs. 16 and 17 show the stress–strain relation for this load combination. Load paths ① and ② are the same as in the previous example (Fig. 13). Before load path ③ starts, the strip is fixed at the end. Due to the heat flux q_0 the temperature in the sample rises. As in the previous example the heating up to the austenite start temperature A_s yields a thermoelastic effect and the sample shows the tendency to expand. Due to the fixation the suppressed longitudinal expansion leads to a negative stress in the sample. When A_s is reached at 263 K, the phase transformation starts. From now on the strip tends to recover its initial shape which generates recovery stress in the sample. Until the end of the applied heat flux q_0 the stress increases linearly. When $\theta_{max} = 327$ K is reached, the stress is about 390 MPa which equals a triple of the maximum stress during the martensite orientation. In load step ④ the sample is cooled down to the initial temperature. At the beginning of the cooling the stress increases up to 400 MPa because of the thermoelastic effect due to w_{ext} in (31). When the martensite start temperature M_s is reached this effect is overlaid by the retransformation from austenite to ori-

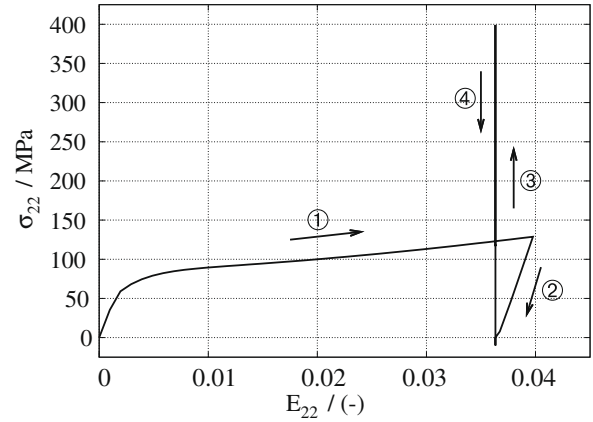


Fig. 16. Stress–strain diagram of the complete loading history (①: loading, ②: unloading, ③: heating, ④: cooling).

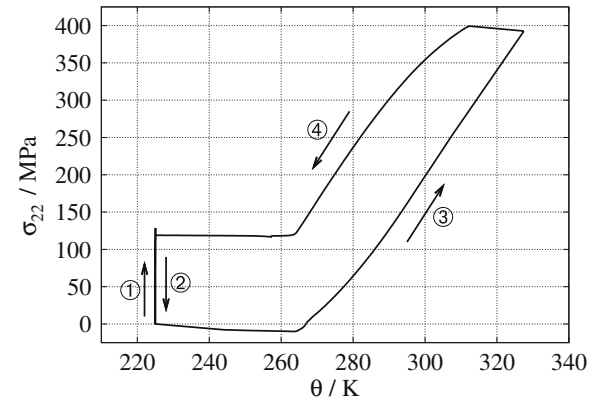


Fig. 17. Stress–temperature diagram of the complete loading history (①: loading, ②: unloading, ③: heating, ④: cooling).

ented martensite and consequently, the stress decreases. When it reaches approximately 125 MPa, the stress level keeps constant since the maximum of the thermally retransformable martensite $z_0 = 0.68$ is reached as is illustrated in Fig. 18. To reproduce the overall maximum of oriented martensite ($z_{0max} = 0.75$) the sample must be mechanically deformed once again up to the load maximum $n_0 = 150$ N/mm². This effect has been experimentally validated by Prahlad and Chopra (2001) who compared their experiments with the constitutive models of Brinson (1993), Liang and Rogers (1990) and Tanaka (1986). The latter models are also capable of describing this phenomenon.

6.2. Shape memory effect in a foot staple

The last example attends to a more practical case. Here, a biomedical foot staple used in foot surgery is presented. The staple is used to fix bone segments after a *phalangeal shortening osteotomy*. This medical intervention reduces the excessive length of the great toe or, it reduces the phalangeal lever arm by cutting the bone into bone segments. Afterwards, the remaining bone segments have to be fixed to help them grow together (Song et al., 2002; Ng et al., 2006). The proposed foot staple has been developed by Krone et al. (2005). It consists of a NiTi alloy and uses the shape memory effect to clamp the bone segments together. The function of the staple is shown in detail in Fig. 19. At first, the initial sample is cooled down below the martensite finish temperature M_f . Then, it is opened mechanically by bending the legs of the staple into the

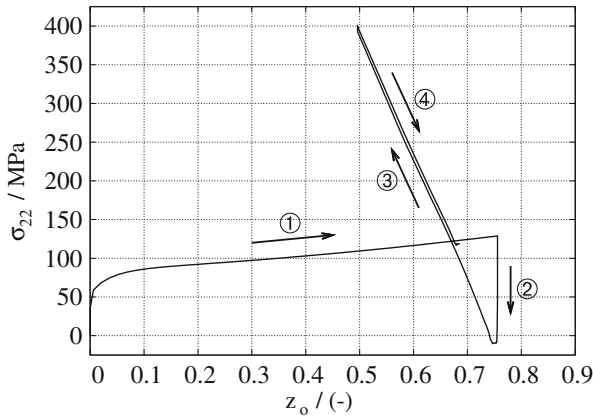


Fig. 18. Stress–martensitic volume fraction diagram of the complete loading history (①: loading, ②: unloading, ③: heating, ④: cooling).

desired position. When the staple is heated above the austenite finish temperature A_f it will recover its original shape if no obstacles are placed between the staple's legs. Inserting obstacles between the legs leads to a clamping effect between the staple and the obstacles. In practice, these obstacles are the bone segments which have to be fixed together. The simulation of this effect requires a comprehensive investigation in order to determine particularly the thermomechanical material parameters.

The significant phase transformation temperatures, $A_{s0} = 260$ K, $A_{f0} = 202$ K, $M_{s0} = 250$ K and $M_{f0} = 230$ K, were deduced via differential scanning calorimetry (DSC) at the NiTi bulk material (Krone et al., 2005). The mechanical parameters can be fitted via a tension test in a temperature regime above A_f and below M_f , respectively (see Fig. 20). The chosen parameters are listed in Table 2. The difference of the internal energy and the entropy can be expressed by (21).

In Fig. 21a the geometry of the staple is defined and its finite element discretisation is illustrated in Fig. 21b. The mesh consists of 872 elements (2 over the thickness, 4 over the height and 109 along the staple legs). Since the staple and the boundary conditions are symmetric, the problem can be reduced to the half. Firstly, the staple is loaded by a distributed force $F = 0.15$ N/mm² on the inner surface of the staple's legs. After unloading the force is replaced by a distributed heat flux $q = 300$ kJ/mm². Both loads are applied in 10,000 s ($\dot{F} = 0.15 \times 10^{-4}$ N/(mm² s) and $\dot{q} = 300 \times 10^{-4}$

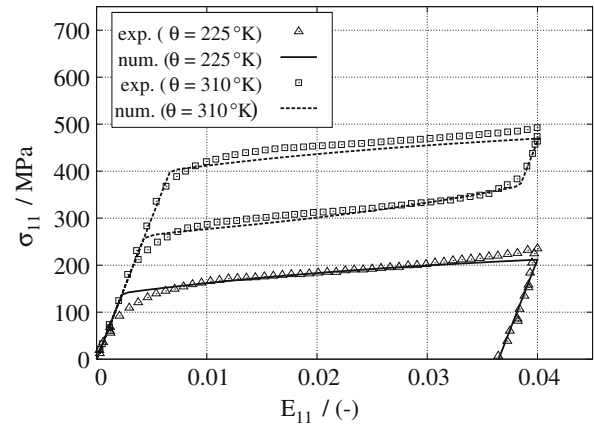


Fig. 20. Stress–strain diagram of a tension test at different temperatures. Comparison of experimental (exp.) and numerical (num.) results.

Table 2
Material parameters for the staple material.

| Parameter | Symbol | Value | Unit |
|---------------------------|-----------------|--------|-------------------|
| Lamé constant | λ | 58,300 | MPa |
| Shear modulus | μ | 22,000 | MPa |
| Kinematic hardening | μ_t | 2000 | MPa |
| Limit of kin. hardening | b | 40 | – |
| Energy difference | Δe_0 | –204 | MPa |
| Entropy difference | $\Delta \eta_0$ | –0.8 | MPa/K |
| Half height of hysteresis | k | 80 | MPa |
| Length of hysteresis | γ | 0.05 | – |
| Density | ρ_0 | 6400 | kg/m ³ |

kJ/(mm² s)), respectively. The following point analyses are taken from the node P at the top of the staple's base (see Fig. 21b).

At first no obstacle is placed between the staple's legs so that a loading–unloading cycle combined with a subsequent heating leads to a free shape memory effect. In Fig. 22, the distribution of the oriented martensite during the opening of the staple is shown. Fig. 22a illustrates the unloaded FE mesh, Fig. 22b the deformed staple at the end of the loading and Fig. 22c the deformed staple after unloading. It can be observed that mainly the backbone of the staple undergoes a martensite orientation. The maximum martensite orientation $z_{0\max} = 0.48$ is achieved at the top of the staple's

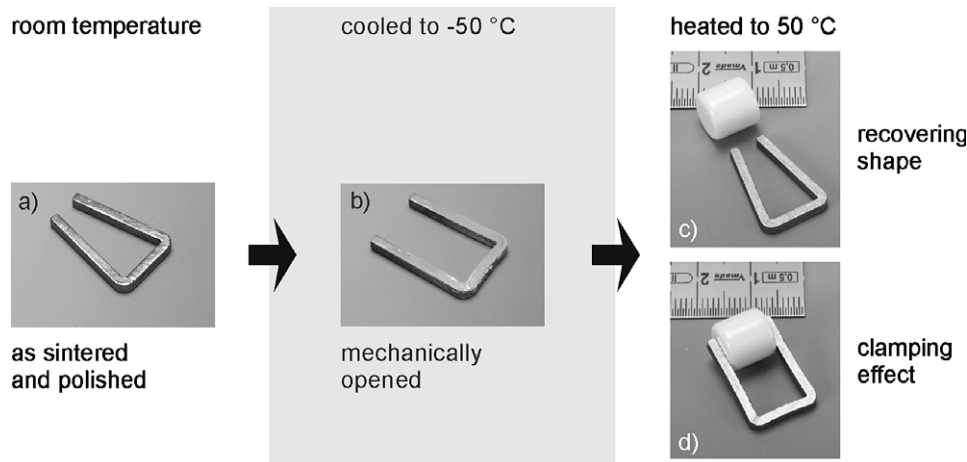


Fig. 19. Function of the NiTi foot staple: (a) initial shape of the staple at room temperature; (b) cooled below M_f and mechanically opened; heated above A_f to (c) recover its initial shape or (d) come into contact with the obstacle.

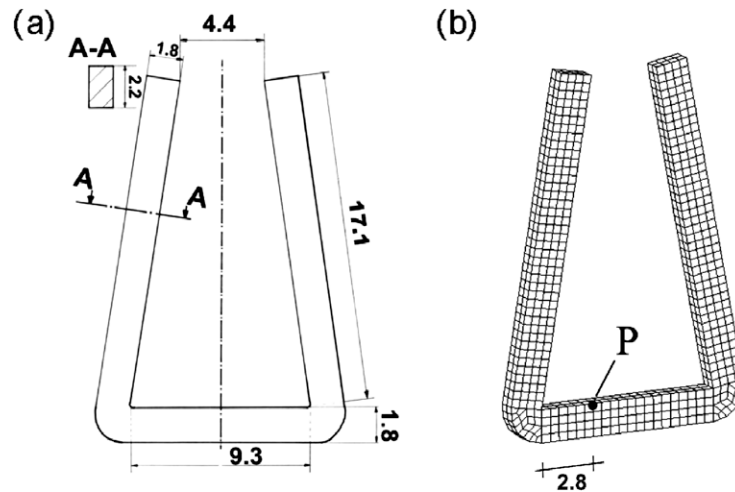


Fig. 21. (a) Geometry (in mm) and (b) FE discretisation of the medical foot staple.

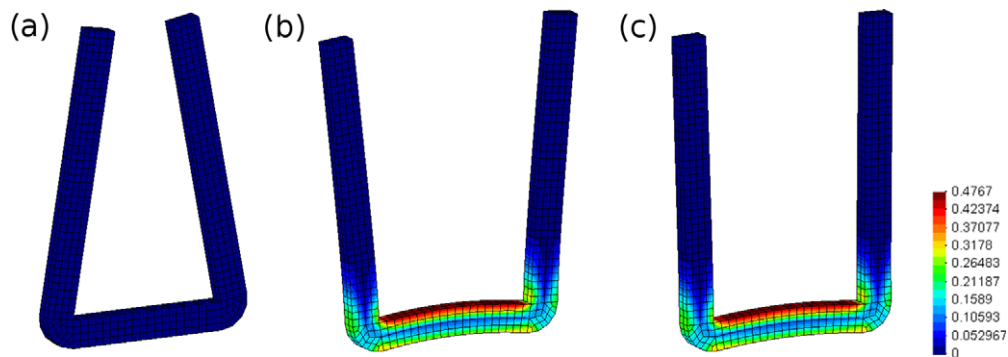


Fig. 22. Distribution of the martensitic volume fraction z_0 during the mechanical opening: (a) at the beginning; (b) at the end of loading; (c) at the end of unloading.

backbone, for instance in point P . An important aspect is that in the center of the backbone no martensite orientation occurs. Because of the bending, the upper part of the backbone is stretched and the lower part is compressed. Consequently, the martensite orientation at the top is tension-dominated and the martensite orientation at the bottom is compression-dominated. Since the scalar factor is set to $m = 0.1$, the tension-dominated region shows a slightly increased martensite orientation. However, the change in

the direction of the orientation yields a neutral axis near the middle of the staple's backbone. Both, the change of sign in stress and the inhomogeneous martensite distribution over the cross section of the staple leads to a specific structural phenomenon which is observable in the stress–strain relation at point P in Fig. 23. Here, it can be observed that after the typical loading path up to a stress maximum of about $\sigma = 195$ MPa, the unloading yields negative stresses at the top of the backbone, with $\sigma = -80$ MPa. Simulta-

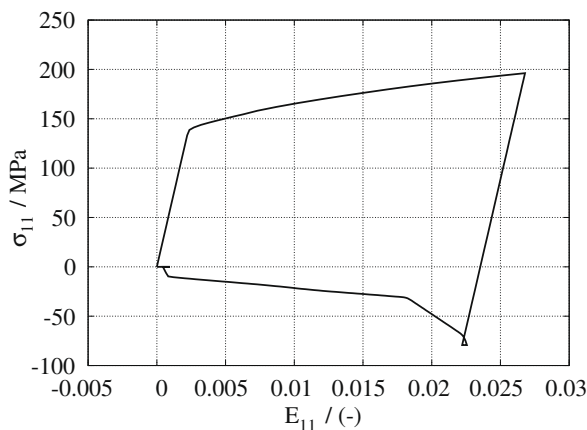


Fig. 23. Stress–strain diagram of the complete loading process (free shape memory effect).

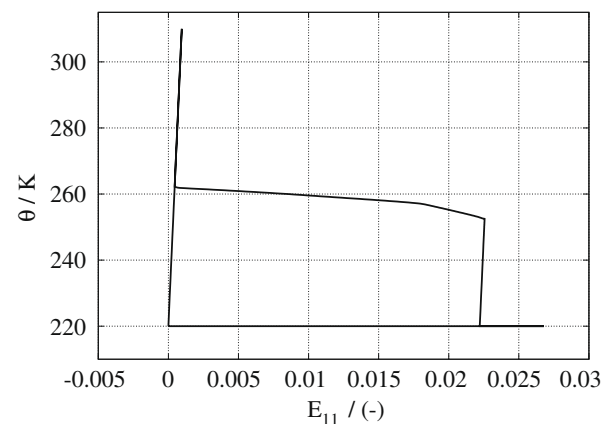


Fig. 24. Temperature–strain diagram of the complete loading process (free shape memory effect).

neously, tension arises at the bottom of the backbone and the remaining stress is balanced after unloading. During the subsequent heating the staple recovers its initial shape and along with it, the internal stress vanishes (see Figs. 23 and 24).

After having investigated the free shape memory effect, we now take a close look at the clamping effect by inserting a bone segment between the staple's legs (see Fig. 25). The segment measures $9.3 \times 18 \times 3$ mm and is discretised by $10 \times 20 \times 2$ elements. Again, the simulation can be carried out using one half of the symmetric mesh. The bone material is modelled via a Neo-Hookean material law with the Lamé constants $\lambda = 94,610$ MPa and $\mu = 63,080$ MPa (see Katz et al., 1984). The bone segment is placed between the legs right after the previous loading–unloading cycle. Then, during the heating phase the staple gets into contact with the bone segment.

In Fig. 25a–c, the deformation of the sample and the distribution of the σ_{11} stress in the sample is plotted for the temperatures $\theta = 220$ K, $\theta = 265$ K and $\theta = 310$ K, respectively. Obviously, during the successive heating the stress increases in the backbone of the staple since the contact with the bone segment makes the shape recovery impossible. In the staple's legs the stress is relatively small. However in Fig. 25c, a stress increase from the middle to the lower part of the legs is visible. To investigate it more profoundly, we cut out only the legs of the staple with the distribution of σ_{11} (Fig. 26). In Fig. 26b ($\theta = 265$ K) and Fig. 26c ($\theta = 310$ K) an increase of the contact stress can be observed. The contact stress is transmitted into the lower part of the legs and the backbone. Interestingly, the contact stress shifts from the upper part to the middle part of the staple. The same can be seen in Fig. 27 where the distri-

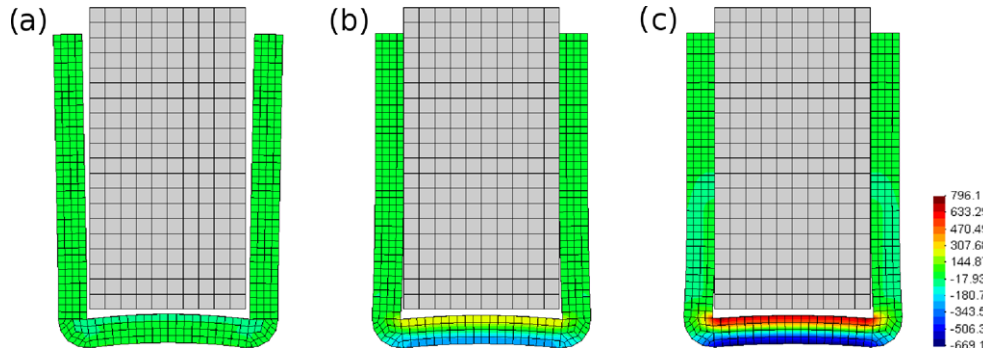


Fig. 25. Distribution of the σ_{11} stress (in MPa) during contact with the bone segment (a) before heating ($\theta = 220$ K); (b) at $\theta = 265$ K; (c) at the end of heating ($\theta = 310$ K).

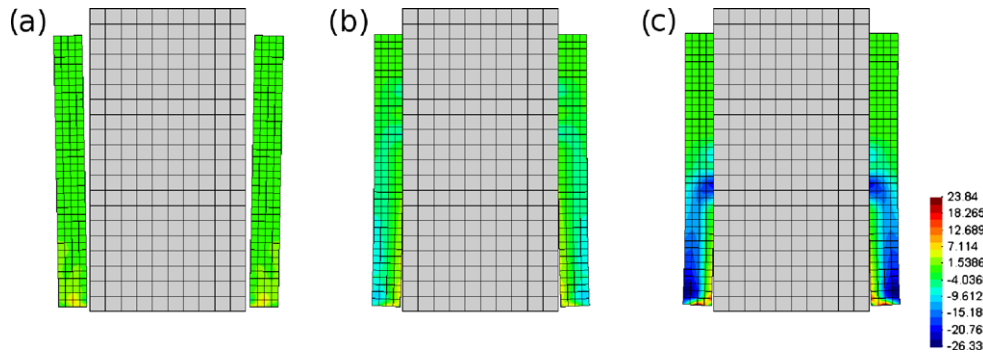


Fig. 26. Distribution of the σ_{11} stress (in MPa) in the staple's legs during contact with the bone segment (a) before heating ($\theta = 220$ K); (b) at $\theta = 265$ K; (c) at the end of heating ($\theta = 310$ K).

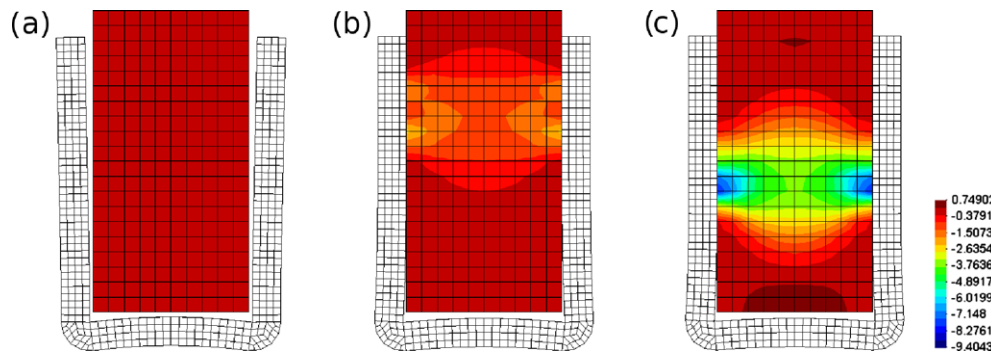


Fig. 27. Distribution of the σ_{11} stress (in MPa) in the bone segment during contact with the staple (a) before heating ($\theta = 220$ K); (b) at $\theta = 265$ K; (c) at the end of heating ($\theta = 310$ K).

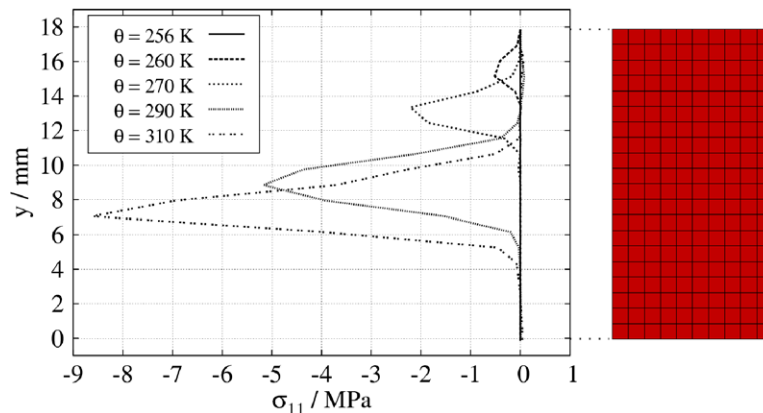


Fig. 28. Evolution of contact stress σ_{11} over the height y of the bone segment at different temperatures.

bution of σ_{11} in the bone segment is visualised at the respective temperatures. By plotting the stress values at the edge of the bone's contact surface over the height y of the bone segment in Fig. 28, the moving stress peak during heating becomes visible. The highest peak is reached at the end of the heating. By integrating the region of the contact stress, a final contact force of $F_{cnum} = 36$ N is achieved. Experimental testing of the staple resulted in a contact force of approximately $F_{cexp} = 33 \pm 1$ N (see Krone et al., 2005). The insignificant difference between the experimental and the numerical results proves the suitability of the model also for complex experiments.

7. Conclusion

This work proposes a new thermomechanically coupled material model for shape memory alloys. We derive the model in the framework of finite strains considering a multiplicative split of the deformation gradient into an elastic and a transformation part. The additional split of the martensitic volume fraction z into unoriented, self-accommodated martensite z_u and oriented martensite z_o allows modelling the pseudoelasticity as well as the shape memory effect. The model is validated on the grounds of a multiaxial experiment whereas the enhanced phase transformation function covers the tension–compression asymmetry in textured NiTi material. To understand the strong thermomechanical coupling phenomena during the phase transformation, an academic example is chosen. Here, the heat production during the phase transformation from austenite to martensite and the shape memory effect under free and restrained conditions is investigated. Finally, the modelling of thermomechanical coupling is validated on the basis of a complex practical example. The medical foot staple, used in the *phalangeal shortening osteotomy*, utilises the shape memory effect to fix bone segments. The detailed experiments on the staple are necessary in order to adjust the material parameters and the final results show an excellent accord of the model and the real behaviour of the material. Finally, we can state that the proposed model is a very complex and accurate model for shape memory alloys which is capable of modelling the most important material behaviours. The formulation of the model in the correct kinematic framework (large strains) and the robust and efficient implementation into a finite element code are very important aspects. Certainly, additional topics such as the training effect in the two way shape memory effect or the fatigue behaviour during cyclic loading are important features which have to be considered as well. However, the structure of this model allows a simple enhancement of the constitutive equations to consider these topics. Particularly, the development of plastic strain after the completed phase transformation can be modelled quite easily by

introducing a further “plastic” deformation gradient \mathbf{F}_p in the multiplicative split of the overall deformation gradient as $\mathbf{F} = \mathbf{F}_e \mathbf{F}_t \mathbf{F}_p$. Since the plastic strain increases to a strain of about 20%, the plasticity cannot be modelled via a small strain formulation.

References

- Achenbach, M., 1989. A model for an alloy with shape memory. *International Journal of Plasticity* 5, 371–395.
- Aleong, D., Dumont, C., Chirani, S.A., Patoor, E., McDowell, D.L., 2002. Transformation surfaces of a textured pseudoelastic polycrystalline Cu–Zn–Al shape memory alloy. *Journal of Intelligent Material Systems and Structures* 13, 783–793.
- Anand, L., Gurtin, M.E., 2003. Thermal effects in the superelasticity of crystalline shape memory materials. *Journal of the Mechanics and Physics of Solids* 51 (6), 1015–1058.
- Armero, F., Simo, J.C., 1993. A priori stability estimates and unconditionally stable product formula algorithms for nonlinear coupled thermoplasticity. *International Journal of Plasticity* 9, 749–782.
- Armstrong, P.J., Frederick, C.O., 1966. A Mathematical Representation of the Multiaxial Bauschinger Effect. Central Electricity Generating Board and Berkeley Nuclear Laboratories, Research & Development Department.
- Auricchio, F., 2001. A robust integration-algorithm for a finite-strain shape-memory-alloy superelastic model. *International Journal of Plasticity* 17, 971–990.
- Auricchio, F., Petrini, L., 2004a. A three-dimensional model describing stress–temperature induced solid phase transformations: thermomechanical coupling and hybrid composite applications. *International Journal for Numerical Methods in Engineering* 61, 716–737.
- Auricchio, F., Petrini, L., 2004b. A three-dimensional model describing stress–temperature induced solid phase transformations: solution algorithm and boundary value problems. *International Journal for Numerical Methods in Engineering* 61, 807–836.
- Auricchio, F., Taylor, R.L., 1997. Shape memory alloys: modelling and numerical simulations of the finite-strain superelastic behavior. *Computer Methods in Applied Mechanics and Engineering* 143, 175–194.
- Bhattacharya, K., 1992. Self-accommodation in martensite. *Archive for Rational Mechanics and Analysis* 120 (3), 201–244.
- Bouvet, C., Calloch, S., LExcellent, C., 2004. A phenomenological model for pseudoelasticity of shape memory alloys under multiaxial proportional and nonproportional loadings. *European Journal of Mechanics A/Solids* 23, 37–61.
- Boyd, J.G., Lagoudas, D.C., 1996. A thermomechanical constitutive model for the shape memory materials. Part I: The monolithic shape memory alloys. *International Journal of Plasticity* 12, 805–842.
- Brinson, L.C., 1993. One-dimensional constitutive behavior of shape memory alloys: thermomechanical derivation with non-constant material functions and redefined martensite internal variable. *Journal of Intelligent Material Systems and Structures* 4, 229–242.
- Christ, D., Reese, S., Neuking, K., 2004. A new finite element technology for shape memory alloy composites. *Materials Science and Engineering Technology* 5, 300–306.
- Dettmer, W., Reese, S., 2004. On the theoretical and numerical modelling of Armstrong–Frederick kinematic hardening in the finite strain regime. *Computer Methods in Applied Mechanics and Engineering* 193, 87–116.
- Eaton-Evans, J., Dulieu-Barton, J.M., Little, E.G., Brown, I.A., 2006. Thermoelastic studies on Nitinol stents. *Journal of Strain Analysis for Engineering Design* 41 (7), 481–495.
- Entermeier, D., Patoor, E., Eberhardt, A., Berveiller, M., 2000. Strain rate sensitivity in superelasticity. *International Journal of Plasticity* 16, 1269–1288.
- Freudenthal, A.M., Gou, P.F., 1969. Second order effects in the theory of plasticity. *Acta Mechanica* 8, 34–52.

- Fu, S., Müller, I., Xu, H., 1992. The interior of the pseudoelastic hysteresis. In: Liu, C., Kunsmann, H., Otsuka, K., Wuttig, M. (Eds.), *Shape-Memory Materials and Phenomena – Fundamental Aspects and Applications*, vol. 246, Materials Research Society Symposium Proceedings, Pittsburgh, Pennsylvania, pp. 39–42.
- Fu, Y., Du, H., Huang, W., Zhang, S., Hu, M., 2004. TiNi-based thin films in MEMS applications: a review. *Sensors and Actuators A* 112, 395–408.
- Gall, K., Sehitoglu, H., 1999. The role of texture in tension–compression asymmetry in polycrystalline NiTi. *International Journal of Plasticity* 15, 69–92.
- Helm, D., 2007a. Thermomechanics of martensitic phase transitions in shape memory alloys. Part I: Constitutive theories for small and large deformations. *Journal of Mechanics of Materials and Structures* 2, 87–112.
- Helm, D., 2007b. Numerical simulation of martensitic phase transition in shape memory alloys using an improved integration algorithm. *International Journal for Numerical Methods in Engineering* 69, 1997–2035.
- Helm, D., Haupt, P., 2002. Thermomechanical representation of the multiaxial behavior of shape memory alloys. *Smart Structures and Materials* 4699, 343–354.
- Helm, D., Haupt, P., 2003. Shape memory behaviour: modelling within continuum mechanics. *International Journal of Solids and Structures* 40, 827–849.
- Hesse, T., Ghorashi, M., Inman, D.J., 2004. Shape memory alloy in tension and compression and its application as clamping-force actuator in a bolted joint. Part I: Experimentation. *Journal of Intelligent Material Systems and Structures* 15, 577–587.
- Van Humbeeck, J., 2001. Shape memory alloys: a material and a technology. *Advanced Engineering Materials* 3 (11), 837–850.
- Huo, Y., Müller, I., 1993. Nonequilibrium thermodynamics of pseudoelasticity. *Continuum Mechanics and Thermodynamics* 5, 163–204.
- Iadicola, M.A., Shaw, J.A., 2004. Rate and thermal sensitivities of unstable transformation behavior in a shape memory alloy. *International Journal of Plasticity* 20, 577–605.
- Idesman, A.V., Levitas, V.I., Stein, E., 1999. Elastoplastic materials with martensitic phase transition and twinning at finite strains: numerical solution with finite element method. *Computer Methods in Applied Mechanics and Engineering* 173, 71–98.
- Kakeshita, T., Shimizu, K., Nakamichi, S., Tanaka, R., Endo, S., Ono, F., 1992. Effect of hydrostatic pressures on thermoelastic martensitic transformations in aged Ti–Ni and a usage Fe–Ni–Co–Ti shape memory alloys. *JIM Materials Transactions* 33, 1–6.
- Katz, J.L., Yoon, H.S., Lipson, S., Maharidge, R., Meunier, A., Christel, P., 1984. The effects of remodeling on the elastic properties of bone. *Calcified Tissue International* 36, 31–36.
- Krone, L., Mentz, J., Bram, M., Buchkremer, H.P., Stöver, D., Wagner, M., Eggeler, G., Christ, D., Reese, S., Bogdansk, D., Köller, M., Esenwein, S.A., Muhr, G., Prymak, O., Epple, M., 2005. The potential of powder metallurgy for the fabrication of biomaterial on the basis of Nickel–Titanium: a case study with a staple showing shape memory behaviour. *Advanced Engineering Materials* 7 (7), 613–619.
- Lagoudas, D.C., Patoor, E., Brinson, L.C., 2006. Shape memory alloys. Part II: Modeling of polycrystals. *Mechanics of Materials* 38, 430–462.
- Leclercq, S., LExcellent, C., 1996. A general macroscopic description of the thermomechanical behaviour of shape memory alloys. *Journal of the Mechanics and Physics of Solids* 44, 953–980.
- Leo, P.H., Shield, T.W., Bruno, O.P., 1993. Transient heat transfer effects on the pseudoelastic behavior of shape-memory wires. *Acta Metallurgica et Materialia* 41 (8), 2477–2485.
- Levitas, V.I., 1998. Thermomechanical theory of martensitic phase transformations in inelastic materials. *International Journal of Solids and Structures* 35, 889–940.
- LExcellent, C., Vivet, A., Bouvet, C., Calloch, S., Blanc, P., 2002. Experimental and numerical determinations of the initial surface of phase transformation under biaxial loading in some polycrystalline shape-memory alloys. *Journal of the Mechanics and Physics of Solids* 50, 2717–2735.
- Liang, C., Rogers, C.A., 1990. One-dimensional thermomechanical constitutive relations for shape memory materials. *Journal of intelligent material systems and structures* 1, 207–234.
- Liang, C., Rogers, C.A., 1992. A multi-dimensional constitutive model for shape memory alloys. *Journal of Engineering Mathematics* 26, 429–443.
- Lim, T.J., McDowell, D.L., 1999. Mechanical behaviour of an NiTi shape memory alloy under axial–torsional proportional and nonproportional loading. *Journal of Engineering Materials and Technology* 121, 9–19.
- Lim, T.J., McDowell, D.L., 2002. Cyclic thermomechanical behavior of a polycrystalline pseudoelastic shape memory alloy. *Journal of Mechanics and Physics of Solids* 50, 651–676.
- Lion, A., 2000. Constitutive modelling in finite thermoviscoplasticity: a physical approach based on nonlinear rheological models. *International Journal of Plasticity* 16, 469–494.
- Liu, Y., Xie, Z., Van Humbeeck, J., Delaey, L., 1998. Asymmetry of stress–strain curves under tension and compression for NiTi shape memory alloys. *Acta Materialia* 46, 4325–4338.
- Masud, A., Panahandeh, M., Auricchio, F., 1997. A finite-strain finite element model for the pseudoelastic behavior of shape memory alloys. *Computer Methods in Applied Mechanics and Engineering* 148, 23–37.
- Matsuzaki, Y., Naito, H., Ikeda, T., Funami, K., 2001. Thermo-mechanical behavior associated with pseudoelastic transformation of shape memory alloys. *Smart Materials and Structures* 10, 884–892.
- Migliavacca, F., Petrini, L., Massarotti, P., Schievano, S., Auricchio, F., Dubini, G., 2004. Stainless and shape memory alloy coronary stents: a computational study on the interaction with the vascular wall. *Biomechanics and Modelling in Mechanobiology* 2, 205–217.
- Müller, C., Bruhns, O.T., 2006. A thermodynamic finite-strain model for pseudoelastic shape memory alloys. *International Journal of Plasticity* 22 (9), 1658–1682.
- Müller, I., Xu, H., 1991. On the pseudoelastic hysteresis. *Acta Metallurgica et Materialia* 39, 263–271.
- Morgan, N.B., 2004. Medical shape memory alloy applications – the market and its products. *Materials Science and Engineering A* 378, 16–23.
- Ng, Y., Shimi, S.M., Kernohan, N., Campbell, P.A., Martin, D., Gove, J., Cuschieri, A., 2006. Skin wound closure with a novel shape-memory alloy fixator. *Surgical Endoscopy* 20, 311–315.
- Otsuka, K., Wayman, C.M., 1999. *Shape Memory Materials*. Cambridge University Press.
- Paiva, A., Savi, M.A., Braga, A.M.B., Pacheco, P.M.C.L., 2005. A constitutive model for shape memory alloys considering tensile–compressive asymmetry and plasticity. *International Journal of Solids and Structures* 42, 3439–3457.
- Patoor, E., Eberhardt, A., Berveiller, M., 1987. Potentiel pseudoelastique et plasticite de transformation martensitique dans les mono- et polycristaux metalliques. *Acta Metallurgica* 35, 2779–2789.
- Patoor, E., Lagoudas, D.C., Brinson, L.C., 2006. Shape memory alloys. Part I: General properties and modelling of single crystals. *Mechanics of Materials* 38, 391–429.
- Pieczyska, E.A., Gadaj, S.P., Nowacki, W.K., Tobushi, H., 2006. Phase-transformation fronts evolution for stress- and strain-controlled tension tests in TiNi shape memory alloy. *Experimental Mechanics* 46, 531–542.
- Popov, P., Lagoudas, D.C., 2007. A 3-D constitutive model for shape memory alloys incorporating pseudoelasticity and detwinning of self-accommodated martensite. *International Journal of Plasticity* 23, 1679–1720.
- Prahlad, H., Chopra, I., 2001. Comparative evaluation of shape memory alloy constitutive models with experimental data. *Journal of Intelligent Material Systems and Structures* 12, 383–395.
- Qidwai, M.A., Lagoudas, D.C., 2000. Numerical implementation of a shape memory alloy thermomechanical constitutive model using return mapping algorithms. *International Journal for Numerical Methods in Engineering* 47, 1123–1168.
- Raniecki, B., LExcellent, C., 1994. RI-models of pseudoelasticity and their specification for some shape memory solids. *European Journal of Mechanics and Solids* 13, 21–50.
- Raniecki, B., LExcellent, C., Tanaka, K., 1992. Thermodynamic models of pseudoelastic behaviour of shape memory alloys. *Archiv Mechanica* 44, 263–284.
- Raniecki, B., Mroz, Z., 2008. Yield or martensitic phase transformation conditions and dissipation functions for isotropic pressure insensitive alloys exhibiting sd effect. *Acta Mechanica* 195 (2), 81–102.
- Raniecki, B., Tanaka, K., Ziolkowski, A., 2001. Testing and modeling of NiTi shape memory alloy at complex stress state. *Material Science Research International* 2, 327–334.
- Reese, S., Christ, D., 2008. Finite deformation pseudo-elasticity of shape memory alloys – constitutive modelling and finite element implementation. *International Journal of Plasticity* 24, 455–482.
- Roubicek, T., 2005. Nonlinear homogenization and its applications to composites, polycrystals and smart materials. In: *Models of Microstructure Evolution in Shape Memory Alloys*, vol. 170. NATO Science Series II: Mathematics, Physics and Chemistry, pp. 269–304.
- Simo, J.C., Miehe, C., 1992. Associative coupled thermoplasticity at finite strains: formulation numerical analysis and implementation. *Computer Methods in Applied Mechanics and Engineering* 98, 41–104.
- Song, C., Campbell, P.A., Frank, T.G., Cuschieri, A., 2002. Thermal modelling of shape memory alloy fixator for medical application. *Smart Structures and Materials* 11, 312–316.
- Souza, A.C., Mamiya, E.N., Zouain, N., 1998. Three-dimensional model for solids undergoing stress-induced phase transformations. *European Journal of Mechanics and Solids* 17, 789–806.
- Tanaka, K., 1986. A thermomechanical sketch of shape memory effect: one-dimensional tensile behavior. *Research Mechanica* 18, 251–263.
- Vieille, B., Michel, J.F., Boubakar, M.L., LExcellent, C., 2007. Validation of a 3D numerical model of shape memory alloys pseudoelasticity through tensile and bulging tests on CuAlBe sheets. *International Journal of Mechanical Sciences* 49, 280–297.
- Vladimirov, I.N., Pietryga, M.P., Reese, S., 2008. On the modelling of non-linear kinematic hardening at finite strains with application to springback-comparison of time integration algorithms. *International Journal for Numerical Methods in Engineering* 75, 1–28.
- Xu, W., Frank, T.G., Stockham, G., Cuschieri, A., 1999. Shape memory alloy fixator system for suturing tissue in minimal access surgery. *Annals of Biomedical Engineering* 27, 663–669.
- Ziolkowski, A., 2007. Three-dimensional phenomenological thermodynamic model of pseudoelasticity of shape memory alloys at finite strains. *Continuum Mechanics and Thermodynamics* 19, 379–398.